On the validity of the Tada stress intensity factor solution for the single edge notch tension specimen with pinned ends

Zachary D. Harris [a,b,*], Joseph W. Cochran [c], Richard P. Gangloff [a], Jacob D. Hochhalter [c], James T. Burns [a]

[a] *Department of Materials Science and Engineering, University of Virginia, Charlottesville, VA, United States*
[b] *Department of Mechanical Engineering & Materials Science, University of Pittsburgh, Pittsburgh, PA, United States*
[c] *Department of Mechanical Engineering, University of Utah, Salt Lake City, UT, United States*

ARTICLE INFO

ABSTRACT

The validity of the Tada stress intensity factor (K_{Tada}) for pinned-ends single edge notch tension [SEN(T)] specimens is assessed via a combined experimental-modeling approach. Analysis of fatigue crack growth rate reductions during constant-ΔK_{Tada} loading demonstrates that specific combinations of alloy stiffness, geometry, and loading result in the true K deviating below K_{Tada}. Geometrically non-linear, 3-dimensional finite element calculations confirm mild-to-strong influences of these parameters, which are not captured by K_{Tada}. Most existing pinned SEN(T) data are found to use parameters where K_{Tada} is not significantly reduced, but the present results underscore the need for a more broadly applicable K solution.

1. Introduction

The single edge notch tension [SEN(T)] specimen was originally proposed by Irwin, Krafft, and Sullivan as an alternative to the notched-round bar for plane strain fracture toughness testing [1–3]. While superseded in current fracture toughness standards [4,5] by the compact tension [C(T)] specimen [6], the SEN(T) is increasingly used to characterize the fracture toughness of reduced-constraint geometries, as well as fatigue crack growth and environment-assisted cracking (EAC) rates. For example, the similarity in the constraint profile of the SEN(T) geometry and an axially cracked pipe wall [7] motivated interest within the oil and gas industry to develop SEN(T)-based fracture toughness measurement standards [8,9]. Regarding EAC and fatigue crack growth testing, the increased use of SEN(T) specimens is driven by several factors. First, the specimen-cracked section is readily isolated in complex environments. Second, the SEN(T) geometry has rigorous-validated analytical relationships [10,11] for crack length measurement *via* the direct current potential difference (dcPD) technique [12,13], which provides automated input for programmed-stress intensity factor (K) loading. Third, the SEN(T) specimen enables studies pertinent to the so-called short/small crack problem in fatigue [14], particularly the role of environment [13,15]. In fact, SEN(T) measurements have elucidated: (a) the effect of short-crack size on the crack tip-chemical environment and associated fatigue crack growth rates (da/dN) [16], (b) transient and steady state da/dN changes in response to environment changes [17–21], (c) fatigue crack growth rates in the ultra-slow loading frequency, long hold time, and near-threshold K regimes where test duration is prohibitively long with the C(T) specimen [13,18,22,23], and (d) wide-range da/dN versus stress intensity range ($\Delta K = K_{max} - K_{min}$) data for jet engine disk and blade fatigue life prediction [24,25]. The SEN(T) specimen

has also been used to characterize crack size, metallurgical, and electrochemical effects on EAC under both sustained and monotonic loading [26–29]. This SEN(T) sample can yield accelerated growth rate data for fracture mechanics prognosis [30], and can incorporate an elastic–plastic J-integral capability [26]. However, broad applications of the SEN(T) specimen demand a validated K solution.

SEN(T) specimens are either threaded, clamped, or pinned into the load train, with each end-fixture condition providing specific advantages. Both clamped and rigidly threaded SEN(T) specimens can be used for tension–compression fatigue experiments; the rigidly threaded condition is more convenient for high temperature testing [31,32]. While the pinned end-fixture setup cannot be effectively used for reversed-load fatigue experiments, the same K is achieved with a significantly reduced applied load relative to the clamped condition [33]. The K solution for each end-fixture condition also results in a unique sample geometry dependence. For example, the clamped SEN(T) K solution is sensitive to the ratio of the distance between the clamping lines (H) and the specimen width (W) [34], which has resulted in numerous proposed K solutions for specific ranges of H/W (reviewed by Zhu [33]). Conversely, the pinned and freely rotating SEN(T) geometry is reported to be insensitive to H/W for all H/W $\geq$ 2 (where H for the rotating SEN(T) geometry is the distance between loading pin centers) [35,36], which led to widespread adoption of the K solution originally proposed by Tada et al. [35]:

$$K_{Tada} = \left(\frac{P}{BW}\right)\sqrt{\pi a}\left\{\sqrt{\frac{2W}{\pi a}tan\left(\frac{\pi a}{2W}\right)}\left[\frac{0.752 + 2.02\left(\frac{a}{W}\right) + 0.37\left(1 - sin\left(\frac{\pi a}{2W}\right)\right)^3}{cos\left(\frac{\pi a}{2W}\right)}\right]\right\} \tag{1}$$

where P is the applied load, B is specimen thickness, W is specimen width, and a is crack length.

Historical studies of pinned SEN(T) specimens yielded reasonable agreement with Eq. 1, albeit with a notable exception for large H/W. Fig. 1a and 1b compare the (a/W) dependencies of dimensionless K, and the difference in K from various authors relative to Eq. 1. Geometrically linear finite element calculations by Joyce et al. [37] and Tokuda and Yamamoto [36] were consistently within 1 % of Eq. 1 for a/W up to 0.8. This excellent agreement was affirmed by a more recent linear finite element analysis of the pinned SEN(T) geometry with H/W of 20 by Hammond and Fawaz [38]. The pinned SEN(T) K solution determined by Gross et al. using the boundary collocation method was also consistently within 1 % of Eq. 1 over the evaluated range of a/W from 0.05 to 0.50 [39]. Other studies reported dimensionless K versus a/W relationships that generally followed the trend of Eq. 1, but at somewhat lower dimensionless K. For example, a coupled experimental-computational study by Sanford and Kirk using the global collocation method informed by photoelastic fringe measurements exhibited a difference with Eq. 1 of between −1 and −5% for 0.1 < a/W < 0.8 [40]. Similarly, though only conducted over 0.15 < a/W < 0.3, half-fringe photoelasticity measurements of Wang et al. indicated a consistent difference of −5% relative to Eq. 1 [41]. Finally, based on a mapping approach [42,43], Emery et al. reported differences from Eq. 1 ranging from −3 to −7% for 0.1 < a/W < 0.62 [44].

Older experimental studies generally agree with Eq. 1 over a somewhat limited range of a/W. Joyce et al. reported similar crack growth (R-curve) resistance behavior for pinned SEN(T) specimens of high strength steel with a/W ranging from 0.35 to 0.65, suggesting K solution (Eq. 1) accuracy for a case where non-linear SEN(T) distortion could be in play [37]. Compliance measurements by Jack [45] on a pinned SEN(T) specimen agreed well with the predictions of Gross et al. for a/W up to 0.5 [39], suggesting concomitant agreement with Eq. 1. Dimensionless K from compliance measurements by Sullivan on AA7075-T6 generally disagree with Eq. 1 at low a/W, with a maximum difference of 30 % at a/W = 0.05, but are within 5 % difference for a/W between 0.3 and 0.5 [2]. Srawley et al. performed compliance measurements on AA7075-T6 SEN(T) specimens, which revealed large deviations from the results of Gross et al. (and therefore Eq. 1) [39] for a/W < 0.2. Srawley et al. recognized that these results are likely not valid due to the extreme challenge in measuring small opening displacements typical of this short crack regime [3]. Interestingly, at larger a/W, this study yielded good
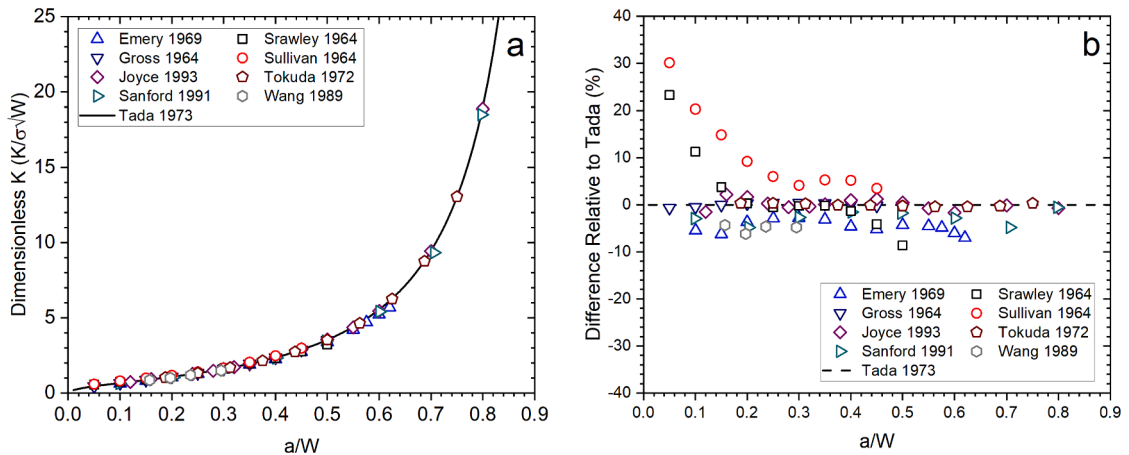

Fig. 1. Comparison of (a) dimensionless K and (b) difference relative to Equation 1 as a function of normalized crack length (a/W) for literature K solutions of the pinned SEN(T) specimen geometry.

agreement with Gross *et al.* over the range $0.2 < a/W < 0.4$, but increasingly poor correspondence for $a/W > 0.4$ (final measurement was at $a/W = 0.5$) [3]. This deviation was attributed to the non-linear eccentricity that loading induced as the pinned SEN(T) geometry rotated open, particularly for longer crack lengths [3]. It was suggested that this yawing action could induce an H/W dependence into the K solution for the pin-loaded SEN(T) [3], as well as possibly reduce K below Eq. 1 due to loading pin friction [46].

An effect of H/W on the SEN(T) K solution is potentially important in studies of environment sensitive fatigue and EAC, as first recognized by Wei and coworkers [47]. They reported a steady 20 to 40 % decrease in crack growth rate (da/dN) with increasing a/W from 0.02 to 0.50 during constant stress intensity range ($\Delta K_{Tada} = K_{max} - K_{min}$) loading of pinned SEN(T) specimens of AA2024-T3 in both dry O_2 and aqueous NaCl. The da/dN decrease with increasing a/W was empirically associated with a decrease in the bracketed geometric term in Eq. 1 (e.g., 0.8 % decrease at a/W of 0.05, 1.5 % at 0.10, 2.5 % at 0.20, 4.0 % at 0.30, 6.6 % at 0.40, and 11.1 % at 0.50). Following Srawley *et al.* [3], Wan *et al.* speculated that this was due to increasingly eccentric loading (and thus reduced net-section bending moment) as the fatigue crack grew in the rotating SEN(T) specimen [47]. Crack closure at the low-employed stress ratio ($R = K_{min}/K_{max} = 0.1$) may have caused part of this da/dN reduction, thus overstating the proposed adjustment to Eq. 1.

Extensive fatigue and EAC studies conducted in the 20 years after the work of Wei and coworkers support the accuracy of Eq. 1 for the pin-rotating SEN(T) specimen, at least for a/W in the range of 0.01 to 0.35 and relatively low employed K values. This work generally showed constant da/dN with increasing crack length during constant ΔK_{Tada}-programmed loading using Eq. 1 [13,17–21,48,49]. Specific results reported for moderate to ultra-high strength steels and Al alloys are detailed in the Discussion. These experiments were designed to minimize growth rate-retarding crack closure and maintain a constant environment during crack growth at constant ΔK. In all cases, the accuracy of Eq. 1 was supported for the pinned SEN(T) geometry with a reduced-section H/W that was high (~10, and perhaps effectively of order 20) due to the tangs used to attach the SEN(T) specimen to clevises.

The validity of Eq. 1 recently again came into question based on fatigue experiments at constant ΔK_{Tada}, supplemented by limited non-linear (geometry) finite element modeling of the pinned SEN(T) specimen with large H/W [50]. Dorman and Fawaz reported a steady reduction in da/dN, by 50 %, with increasing a/W from 0.1 to 0.6 during constant ΔK_{Tada} loading at constant stress ratio ($R = 0.65$) using pinned SEN(T) specimens (reduced section $W = 10$ mm and $H/W = 10$ to 20) of AA7075-T651 stressed at a frequency of 1 Hz in laboratory air [50]. Dorman and Fawaz reported the same declining da/dN behavior for 40 fatigue experiments with SEN(T) specimens [51]: (a) taken from different locations in the thick plate, (b) fabricated by different shop methods, (c) with different notch dimensions, (d) with different pin sizes, (e) tested by different personnel, and (f) for an electrically isolated specimen in the dcPD circuit. By elimination, Dorman and Fawaz concluded that da/dN decreased with increasing a/W because ΔK_{Tada} was under-predicted by Eq. 1 for large H/W due to the non-linear SEN(T) geometry influences [50]. To test this hypothesis, a single linear-elastic, non-linear geometry finite element calculation was conducted with the actual employed SEN(T) geometry [50]. The results of this calculation indicated that the true K for the tested aluminum alloy was 30 % lower than that predicted from Eq. 1 at an a/W of 0.50. Such a result was notably higher than the empirically-based reduction in K of 11 % estimated by Wan et al. for their testing geometry at a/W of 0.5 [47], suggesting a potential synergistic effect from loading, geometry, and alloy parameters.

This literature review establishes that: (1) the pinned-rotating SEN(T) specimen is an important tool in modern experimental studies of environment-sensitive fatigue and EAC, (2) K from many geometrically-linear finite element analyses are consistently within 1 % of Eq. 1, and (3) a wide range of experimental studies using Eq. 1 yielded results that affirm this stress intensity solution, particularly at low-to-moderate a/W. However, results by Srawley *et al.* [3], Wei and coworkers [47], and Dorman and Fawaz [50] show that real K can be between 5 % and 30 % less than that given by Eq. 1. The magnitude of this deviation appears to increase with increasing SEN(T) H/W and a/W, as well as with decreasing load-train and specimen stiffness; factors that interact to increase the eccentricity of the load-line relative to the mid-point of uncracked net section [3]. Given the widespread use of the pinned SEN(T) specimen geometry (and therefore Eq. 1), both in past and on-going studies, this potential impact of such non-linear influences on K_{Tada} strongly motivates a detailed reexamination of Eq. 1 and its validity.

The objective of this study is to evaluate the accuracy of the elastic-K_{Tada} solution (Eq. 1) for the pinned SEN(T) geometry, and to inform the direction of future modifications that account for non-linear geometry changes, via a combined experimental-computational approach. Constant ΔK_{Tada} fatigue experiments are performed on Al, Ti, and Fe-based alloys to assess the evolution of da/dN as a function of a/W. The trends observed in these experimental data are compared to literature crack growth rate data. This combined database is then interpreted using finite element simulation results, both geometrically linear and non-linear, conducted over a large SEN(T) geometry, uncracked ligament size, loading configuration, and material variable space.

2. Experimental methods

2.1. Materials

Seven alloys were evaluated in this study, including: (1) 17-4PH stainless steel in the H1025 temper [52], (2) Custom 465 stainless steel in the H900 temper [53], (3) an experimental CrNiMoV martensitic steel [53], (4) 316L stainless steel in the cold-worked condition, (5) AA7075 in the T651 temper[54], (6) AA5456 in the H116 temper [55], and (7) Beta-C titanium in the solution-treated and aged (ST/A) condition [56]. Each alloy, except for 316L, was evaluated in prior studies by the authors; relevant material processing and sample extraction details, mechanical properties, and composition data are cited in the references above. 316L was procured as a cold worked 16-mm diameter bar. Supplier-reported yield strength was 545 MPa, ultimate tensile strength was 680 MPa, reduction in area was 69.1 %, and composition (in wt.%) was 16.61 % Cr, 10.55 % Ni, 2.04 % Mo, 1.32 % Mn, 0.46 % Cu, 0.31 % Co, and 0.017 % C, with the balance being Fe.

2.2. Fatigue crack growth experiments

For each material, SEN(T) specimens were extracted directly from the material stock; the flat-gage section width (W) and thickness (B), H/W ratio (where H is defined as the distance between the loading pins in the clevis configuration), initial notch length (a_0), and specimen orientation for each alloy are summarized in Table 1. The X-Y sample orientation convention is used, where X is the material stock direction parallel to the loading axis and Y is the material direction parallel to the Mode I crack growth direction. For all materials, a starter notch with height of 38 μm was introduced into each sample at the mid-height of the gage section using electrical discharge machining. The initial notch depth for each specimen was measured on each face of the gage section using a calibrated Hirox RH8800 digital microscope and then averaged to obtain a_0, while W and B were determined using digital calipers.

Fatigue crack growth experiments were performed on pin-loaded SEN(T) specimens using a servo-hydraulic mechanical load frame operated with Fracture Technology Associates FCGR software. The freely rotating end condition was met *via* clevis-based loading, where the SEN(T) specimen with threaded ends was screwed into tangs that were pin-fastened into clevises connected to very rigid load frame crosshead and actuator. The pins, clevises, and tangs were all machined from 17-4PH-H900. A schematic of the test configuration is shown in Fig. 2.

After being placed in the mechanical load frame, each specimen was aligned with the clevises to allow for free rotation, in compliance with the boundary conditions of Eq. 1 [35]. All experiments were conducted in laboratory air at ambient temperature using a fixed stress ratio, R, fixed ΔK_{Tada} loading protocol, where the applied load was actively reduced based on continuous measurements of growing crack length. Details of the experiments are provided in Table 2.

The subcritical-growing crack length during each experiment was measured using the direct current potential difference (dcPD) technique [12,13] with a constant current (4.000 A for Fe-based alloys, 6.000 A for Al alloys, and 2.000 A for Ti alloys) applied through 10-gage copper wires attached to the 17-4PH tangs. Voltage measurements were taken using 36-gage alumel or copper wires (depending on the tested alloy; Al alloys used copper wire) that were spotwelded ~ 0.5 to 0.7 mm above and below the EDM notch. These voltage values were converted to crack length using Johnson's equation [10] where the adjustable constant (V_0) was the potential associated with the initial notch length. Each potential measurement was corrected for thermally-induced voltages using current polarity reversal, with the average of approximately 500 individual voltage readings utilized per individual crack length measurement. The da/dN was calculated from crack length versus cycle count data using the incremental (n = 3) polynomial method outlined in ASTM E647-15e1 [57]. Once the targeted-final a/W was reached, each specimen was fractured under displacement control.

2.3. Finite element modeling

Two finite element models were considered in this study. The first of these being the experimental test geometry detailed in Section 2.2, including tang grips and SEN(T) specimen; this model is referred to as the real SEN(T). The second model was an idealized dog bone specimen that captured the gauge region of the real SEN(T) specimen with similar pinned ends (Fig. 3). This idealized geometry allowed multiple values of H/W to be readily assessed and enabled direct comparison to past research as this geometry is more generalized. Three representative material systems were modeled: AA7075-T651, ST/A Beta-C Ti, and Inconel 718 with Young's moduli of 75, 100, and 200 GPa, respectively, to cover the full range of alloy stiffness.

Initial (uncracked) SEN(T) geometries, boundary conditions, linear-elastic material properties, and geometrically linear or nonlinear analysis of the 3D finite element models were defined in Abaqus [58]. Franc3D (F3D) was used to insert straight through cracks (analogous to previous 2D models) and compute K along the crack front using the M−Integral [59] with stress and strain fields computed by Abaqus. Franc3D works by inserting cracks that are entirely embedded within the geometry (i.e., not on an external face) so the full geometry was modeled without simplifying symmetries. Prior to inserting the crack, each model was subdivided into coherent global and local domains (Fig. 4), which reduced remeshing to only the local model (i.e., only near the crack), while the global model mesh remained unchanged. This approach improved performance (via simplified remeshing steps) and provided improved control over mesh refinement near and coarsening away from the crack. The M−Integral method was used because it improves accuracy over alternatives such as displacement correlation or virtual crack closure methods [60]. Tada likely employed a 2D finite element analysis that used weight function displacements to calculate K, leading to Eq. 1 [35].

Crack front elements were selected to be ¼-point wedge elements to model the stress singularity, which are surrounded by quadratic hexahedra (Fig. 4) to form a crack front template that is used to improve the accuracy of the computed K values. Outside the crack front template, quadratic tetrahedra constituted the remainder of the local and global domains, see Fig. 4. To mitigate any influence of numerical parameters on K, a convergence study identified the requisite mesh refinement and crack growth increments

Table 1
SEN(T) geometry and orientation parameters for each tested alloy.

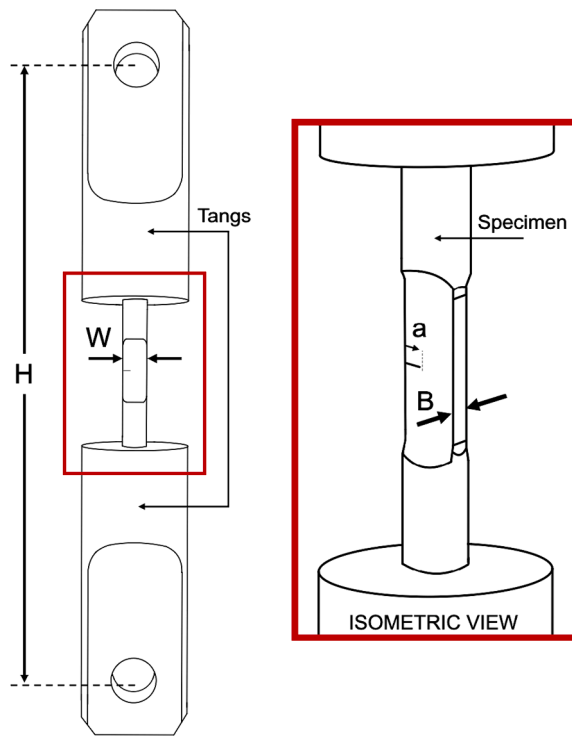| Material	B (mm)	W (mm)	a_0 (mm)	H/W	Sample Orientation
17-4PH (H1025)	2.65	12.2	0.93	24	L-T
Custom 465-H900	2.65	10.2	0.2	29	L-R
CrNiMoV	2.65	10.2	0.2	29	N/A
AA5456-H116	6.60	17.25	1.5	14	S-T
AA7075-T651	2.65	10.1	0.2	29	L-T
316L (CW)	2.65	12.2	0.94	29	L-R
Beta-C (ST/A)	2.65	12.2	2.25	29	L-R

Fig. 2. SEN(T) specimen and model geometry with zoomed isometric view for detail.

Table 2
Overview of fatigue testing parameters for each alloy.

Material	Precracking Protocol	Test ΔK (MPa$\sqrt{m}$)	R	a/W Range
17-4PH (H1025)	Constant ΔK = 6.3 MPa$\sqrt{m}$ at R = 0.1 from a_0 to 1.18 mm	9.0	0.5	0.1 to 0.8
Custom 465-H900	None; tested directly out of notch	10.0	0.65	0.1 to 0.85
CrNiMoV	None; tested directly out of notch	10.0	0.65	0.1 to 0.9
AA5456-H116	None; tested directly out of notch	5.0	0.5	0.1 to 0.8
AA7075-T651	None; tested directly out of notch	6.0	0.65	0.1 to 0.9
316L (CW)	Constant ΔK = 6.5 MPa$\sqrt{m}$ at R = 0.1 from a_0 to 1.19 mm	7.0	0.7	0.15 to 0.75
Beta-C (ST/A)	Constant ΔK = 10.8 MPa$\sqrt{m}$ at R = 0.1 from a_0 to 3.75 mm	15.0	0.5	~0.30 to 0.77

across the a/W domain. Convergence was determined to occur with a crack-front characteristic edge length of 0.125–0.5 mm, with approximately 20 quadratic elements through thickness, depending on the overall model size. The aspect ratio (H/W) for the idealized models, where H is defined as the distance between pins, was modeled as 8, 16, and 29, whereas the true specimen geometry had an H/W of approximately 23. For all idealized model cases, a/W ranged from 0.1 to 0.9. For the true SEN(T), a/W ranged from 0.2 to 0.9.

The defined boundary conditions annotated in Fig 5 represent a frictionless pin-loaded coupon. Specifically, boundary conditions were defined at a reference point node at the pinhole center, which was then tied to a geometric surface or node-set. The reference point boundary condition included a vertically applied load (P) which remained vertical throughout the simulation. The specimen was free to rotate about the top and bottom pins (about the z axis, UR3).

3. Results

3.1. Constant ΔK_{Tada} fatigue experiments

Measured fatigue crack growth rate versus a/W relationships for a CrMoNiV steel, Custom 465, 316L, and 17-4PH in the H1025 temper under various constant ΔK_{Tada} and R are shown in Fig. 6a-d, respectively. The four experiments broadly exhibit one of three behaviors. First, CrMoNiV (Fig. 6a) loaded at ΔK_{Tada} = 10 MPa$\sqrt{m}$ and R = 0.65 exhibited constant da/dN over the range of tested a/W, with variations consistent with typical scatter in fatigue crack growth data [61,62]. Second, and conversely, the 316L specimen loaded at constant ΔK_{Tada} = 7 MPa$\sqrt{m}$ and R = 0.7 exhibits a continually decreasing da/dN over the tested a/W range (Fig. 6d). Third, Custom 465 (Fig. 6b) and 17-4PH (Fig. 6d) exhibit constant da/dN up to a/W of 0.65 and 0.70, respectively, after which measured da/dN declines.
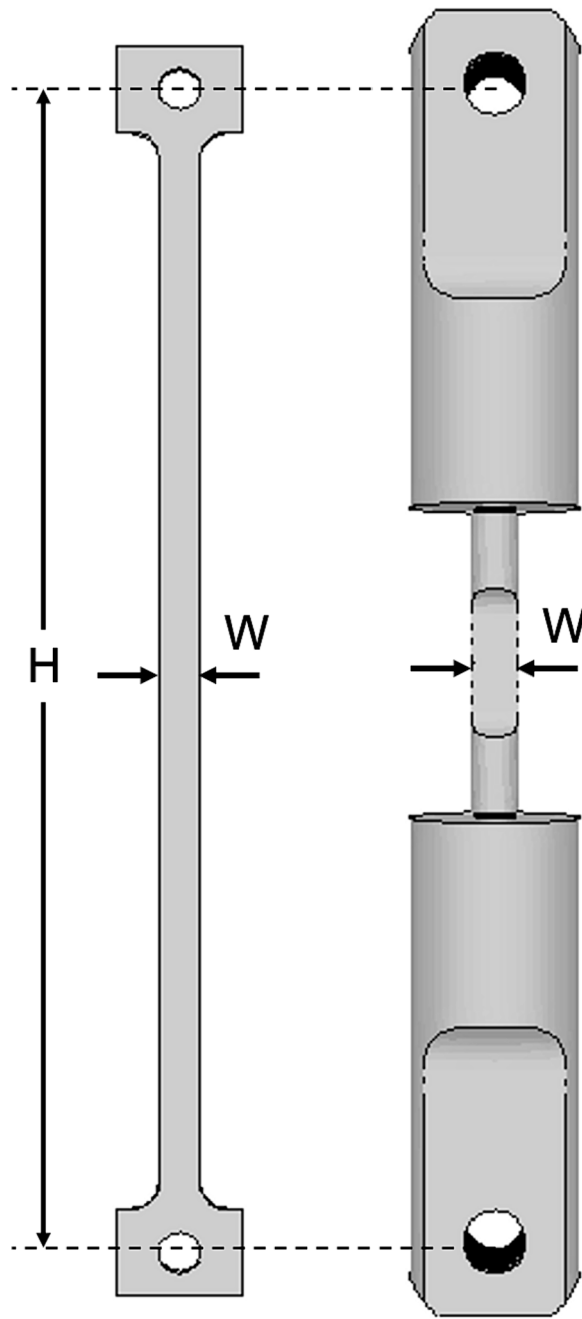
Fig. 3. Idealized model geometry (left) and real SEN(T) model geometry (right).

Similar crack growth rate variations were observed during constant ΔK_{Tada} loading of AA7075-T651 and AA5456-H116, shown in Fig. 7a and b, respectively. The AA7075 specimen tested at $\Delta K_{Tada} = 6$ MPa$\sqrt{m}$ and R = 0.65 exhibited constant da/dN, with local variations and over a broad a/W range, followed by a sharp increase in da/dN as a/W approached 0.9. Speculatively, for very long crack depths, variability in the very low applied force (~10 to 20 N) induced non-negligible errors in applied ΔK_{Tada}, causing the accelerated da/dN in Fig. 7a. The AA5456-H116 tested at $\Delta K_{Tada} = 5$ MPa$\sqrt{m}$ and R = 0.5 exhibited mildly increasing da/dN over a large a/W range, as shown in Fig. 6b. However, counter to AA7075-T651, AA5456-H116 exhibited a decrease in da/dN after a/W = 0.7, similar to the behavior noted for the 17-4PH steel in Fig. 6d. Neither aluminum alloy exhibited steadily declining da/dN with increasing a/W, as reported by others [47,50,51].

An experiment conducted on ST/A Beta-C at constant $\Delta K_{Tada} = 15$ MPa$\sqrt{m}$ (R = 0.5) exhibited a significant decline in da/dN. As shown in Fig. 8, da/dN immediately begins to decrease as the experiment is initiated, followed by an inflection to an even steeper
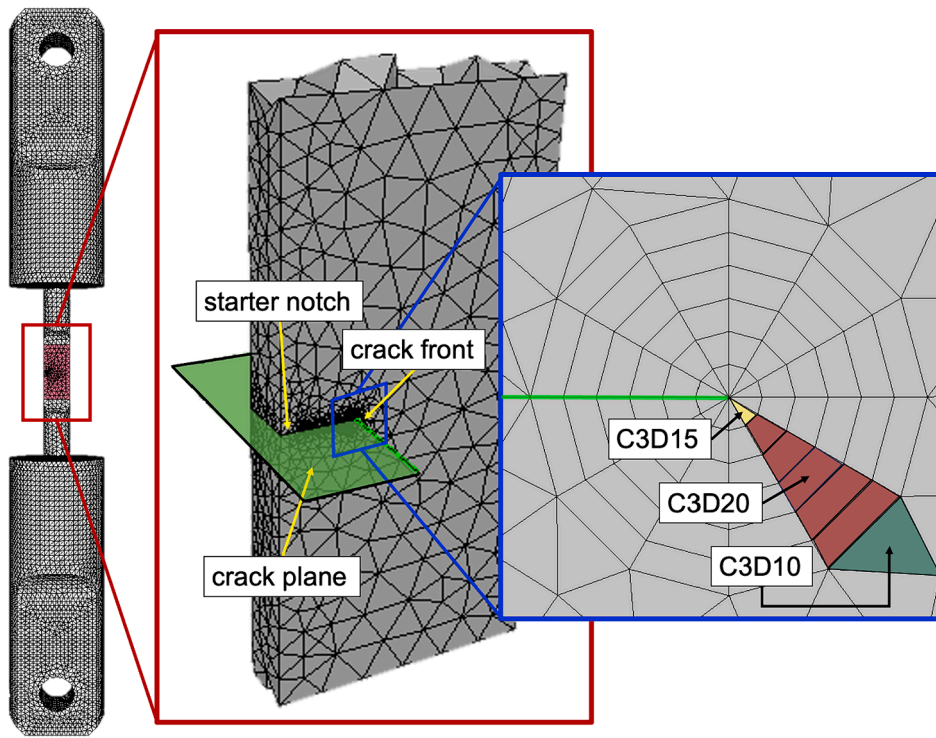
Fig. 4. Global model for the real SEN(T), local model with an inserted crack, and a magnified view of the crack front template rosette with surrounding element annotations.
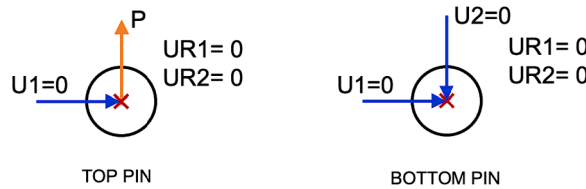

Fig. 5. Boundary conditions enforced for top (left) and bottom pins (right). Boundary conditions applied through reference points are depicted by red X's. (For interpretation of the references to color in this figure legend, the reader is referred to the web version of this article.)

decline in da/dN at a/W > 0.6. In total, da/dN decreases by more than an order of magnitude, which is significantly larger than the deviations noted for the other experiments in this study (Figs. 6 and 7), as well as those reported in the literature and summarized in the Discussion.

3.2. Finite element analysis

Geometrically linear, plane-strain FEA – to establish a comparative baseline between 3D FE results and Eq. 1, we impose plane-strain boundary conditions on the FE model for consistency with Tada's 2D plane-strain model. Plane-strain boundary conditions on the 3D model were imposed by constraining the z-displacement (U3 = 0) on front and back faces of the idealized specimen model. The results of this study are shown in Fig. 9 for an H/W of 8, illustrating an average K_{FE} within ±1% of K_{Tada}. The results are independent of H/W, so the consistency of K_{FE} and K_{Tada} persists for all H/W, so long as linear geometry with plane strain conditions is enforced in the FE model. In the following FE models studied, the plane-strain boundary conditions were not enforced, to model the crack front constraint more accurately, i.e., the 3D FE model does not require such an assumption.

Geometrically linear FEA – because of the focus on fatigue applications in this research we present results in terms of ΔK, i.e., K_{max} − K_{min}. To calculate the percent difference between ΔK_{FE} and ΔK_{Tada} we must assume the load ratio for simulation, R_{FE}, is equal to the load ratio obtained using Eq. 1, R_{Tada}. To align with experiment, a load ratio of 0.65 was used. The percent difference, Eq. 2, between ΔK_{FE} and ΔK_{Tada} is shown in Fig. 10a-c and observed to vary between 7 and 10 %. The solid lines in Fig. 10a-c illustrate the difference defined by Eq. 2 at the center of the crack front and shaded portions indicate the variation in the computed ΔK_{FE} along the 3D crack front. The percent difference is relatively insensitive to changes in a/W and is due to the removal of the plane-strain boundary
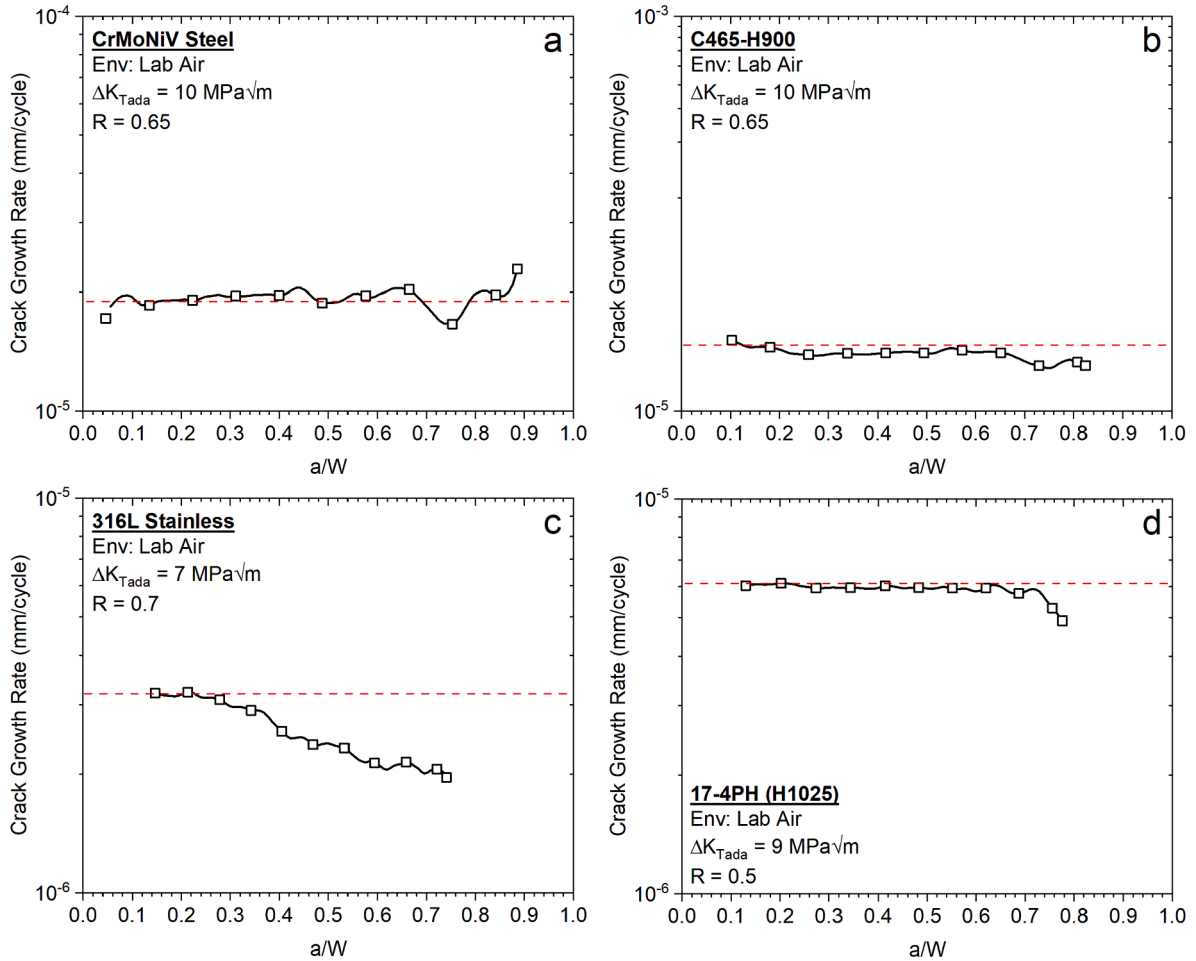
Fig. 6. Measured fatigue crack growth rate as a function of normalized crack length (a/W) during constant ΔK_{Tada} loading in laboratory air for SEN (T) specimens of (a) an experimental CrMoNiV alloy, (b) Custom 465, (c) cold-worked 316L, and (d) 17-4PH. The red dashed line corresponds to a constant da/dN as a function of a/W. (For interpretation of the references to color in this figure legend, the reader is referred to the web version of this article.)

condition in the 3D FE model. Essentially, this difference represents the error in Eq. 1 from the plane-strain assumption. Additionally, the computed ΔK_{FE} results are independent of load and H/W, which is consistent with the reviewed literature.

$$difference\ relative\ to\ Tada\ (\%) = \left(\frac{\Delta K_{FE} - \Delta K_{Tada}}{\Delta K_{Tada}}\right) * 100 \qquad (2)$$

Geometrically nonlinear FEA – lastly, the difference between ΔK_{FE} and ΔK_{Tada} (for R = 0.65) with geometrically nonlinear FEA is illustrated in Fig. 10d-f. As with Fig. 10a-c, the solid lines in Fig. 10d-f illustrate the difference defined by Eq. 2 at the center of the crack front and shaded portions indicate the variation in the computed ΔK_{FE} along the 3D crack front. These results indicate a clear dependence of ΔK_{FE} on P, a/W, and H/W, which differs from previous geometrically-linear FE results and Tada (Eq. 1) [35–37]. Specifically, geometrically nonlinear FE results show that: (1) corresponding ΔK_{FE} decrease sharply as a/W increases with respect to ΔK_{Tada}, and (2) this effect is amplified with increasing H/W or P.

Conventionally, stress intensity factors are a function of specimen geometry and loading, but not material properties [63]. However, the results in Fig. 10 clearly indicate that the geometrically non-linear results increasingly differ from the idealized-linear ΔK_{FE} (and Eq. 1) upon increased yawing (i.e., increased a/W, H/W, and P). The geometrically linear finite element approximation over-predicts yawing and eccentric loading, as does Eq. 1 and the supporting models shown in Fig. 1. Overpredicted yawing and eccentric loading result in higher-predicted ΔK_{FE} values or, in other words, underpredicted load required to achieve a desired ΔK_{Tada}. Since material stiffness influences the degree of yawing, it follows that an underlying ΔK_{FE} dependence on material-elastic properties exists.

Consequently, any material-stiffness dependence of the computed K_{FE} was assessed using the geometrically non-linear FE analysis. To test this, the effect of elastic modulus (E) varying ranging from 75 GPa (Al) to 200 GPa (Ni and Steel) was modeled with the real SEN (T) geometry because it is most pertinent for comparison to experimental results (Table 1 and Table 2). Note, for this comparison K_{FE}
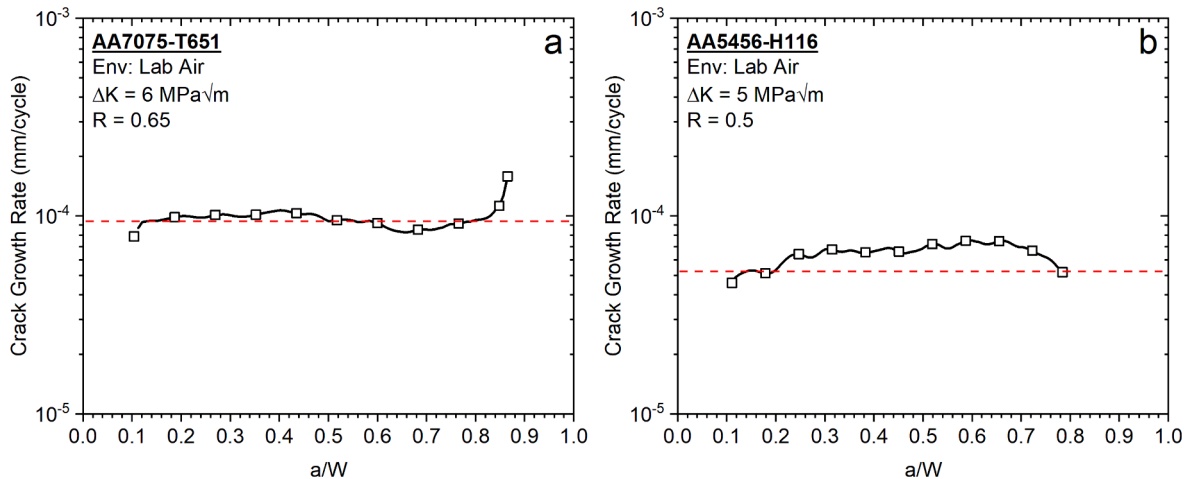
Fig. 7. Measured fatigue crack growth rate as a function of normalized crack length (a/W) during constant ΔK_{Tada} loading in laboratory air for SEN (T) specimens of (a) AA7075-T651 and (b) AA5456-H116. The red dashed line corresponds to a constant da/dN as a function of a/W. (For interpretation of the references to color in this figure legend, the reader is referred to the web version of this article.)

Fig. 8. Measured fatigue crack growth rate as a function of normalized crack length (a/W) for a solution-treated and aged (ST/A) Beta-C titanium SEN(T) specimen in laboratory air loaded at R = 0.5 and a constant $\Delta K_{Tada} = 15$ MPa$\sqrt{m}$. The red dashed line corresponds to a constant da/dN as a function of a/W. (For interpretation of the references to color in this figure legend, the reader is referred to the web version of this article.)
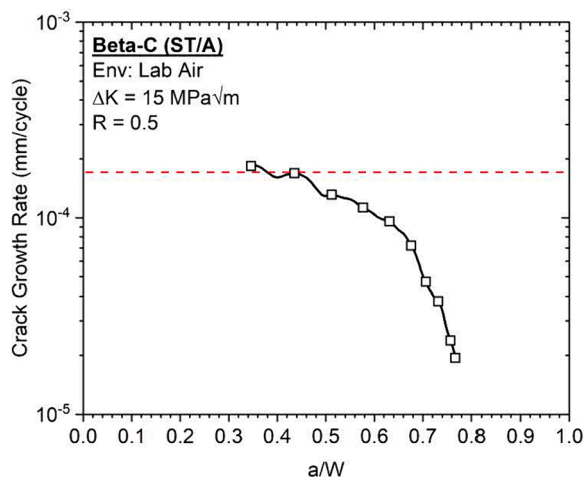
and K_{Tada} are explored (in lieu of ΔK) to directly assess percent differences in the SIF solutions. Consistent with the experimental setup (Section 2.2), the threaded tang material was always 17-4PH in the H900 temper. Modeling the real geometry means that H/W remains fixed at the measured value, while a/W and load are varied. Non-linear FE simulations were completed, with loads ranging from 0.04 to 12.5 kN and a/W ranging from 0.1 to 0.9, producing a broad range of K_{FE} data points. Fig. 11a-d illustrates a contour of this relative difference across the range of P and a/W values for each elastic modulus, 75 GPa (Fig. 11a,c) and 200 GPa (Fig. 11b,d). A cyan line indicates where the relative difference equals zero. The annotated white line on each of the contour plots represents an isoline of constant K_{Tada} with $K_{Tada} = 17$ MPa$\sqrt{m}$ in Fig. 11a,b and $K_{Tada} = 30$ MPa$\sqrt{m}$ in Fig. 11c,d. Finally, the relative difference along these white isolines is illustrated in Fig. 11e-f. Comparing constant K values, the differences observed between the model results in Fig. 11e (for 70 GPa) and Fig. 11f (for 200 GPa) demonstrate that there is an underlying ΔK_{FE} dependence on material-elastic properties that is most potent at higher a/W.

4. Discussion

The preceding experimental and computational results demonstrate that material/geometry/loading combinations exist that result in Eq. 1 no longer being an accurate description of the K solution for the rotating SEN(T) coupon. Conversely, these results also reveal that there are combinations where Eq. 1 does accurately describe the K solution for the pinned SEN(T). The objective of the following
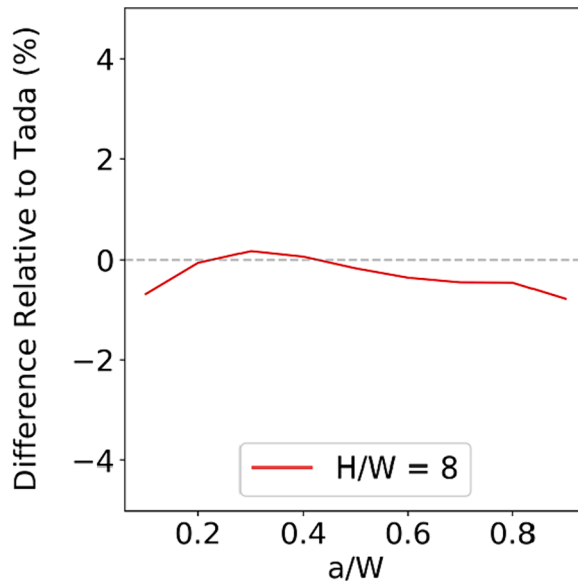
Fig. 9. Comparison of the difference between K_{FE} to K_{Tada}, relative to K_{Tada} (Eq. 2), as a function of normalized crack length (a/W) for specimen geometry of h/W = 8 and E = 75 GPa with added plane-strain boundary condition.
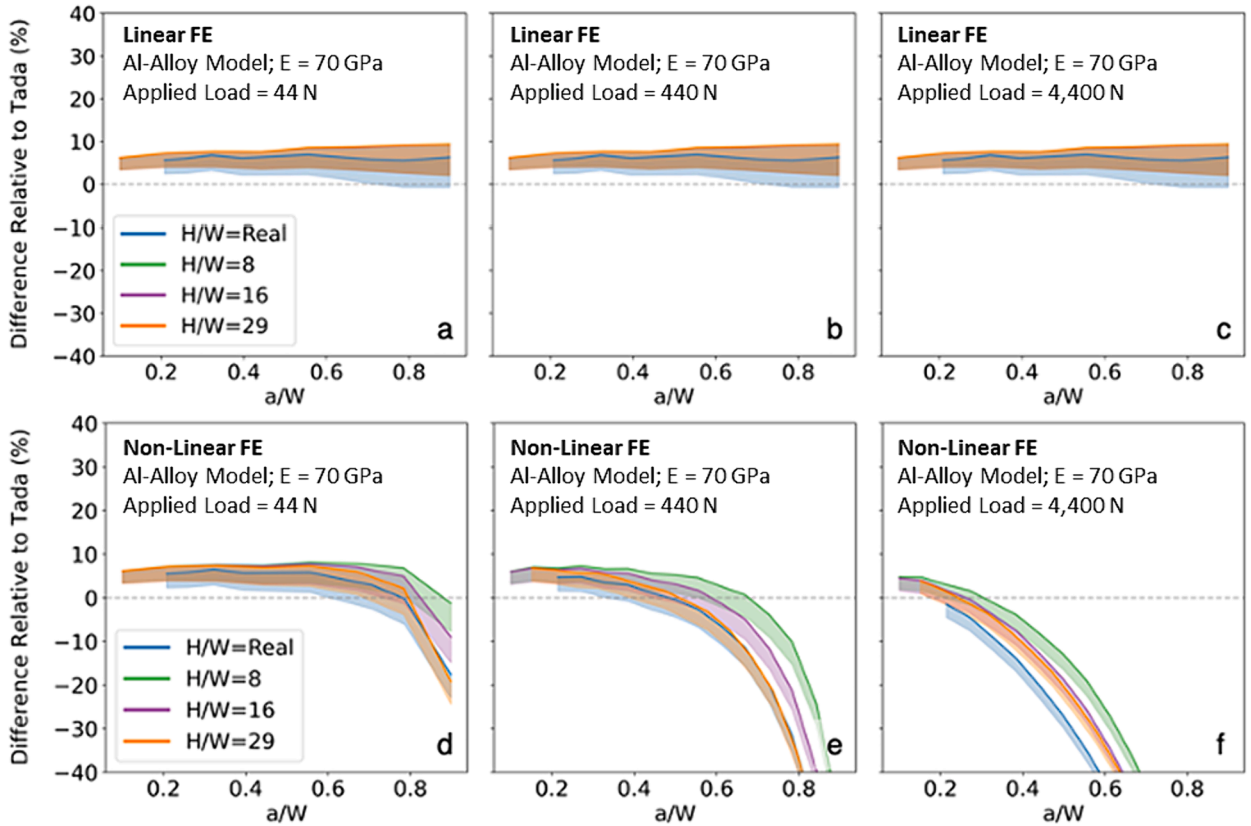

Fig. 10. Comparison of the difference between ΔK_{FE} and ΔK_{Tada}, relative to ΔK_{Tada} at R = 0.65 (Eq. 2) as a function of a/W, load, and H/W. Linear FE is shown on the top row (a-c), and non-linear FE on the bottom row (d-f). The applied load is 44 N (a,d), 440 N (b,e), 4400 N (c,f), with an Al alloy model (E = 70 GPa). (For interpretation of the references to color in this figure legend, the reader is referred to the web version of this article.)
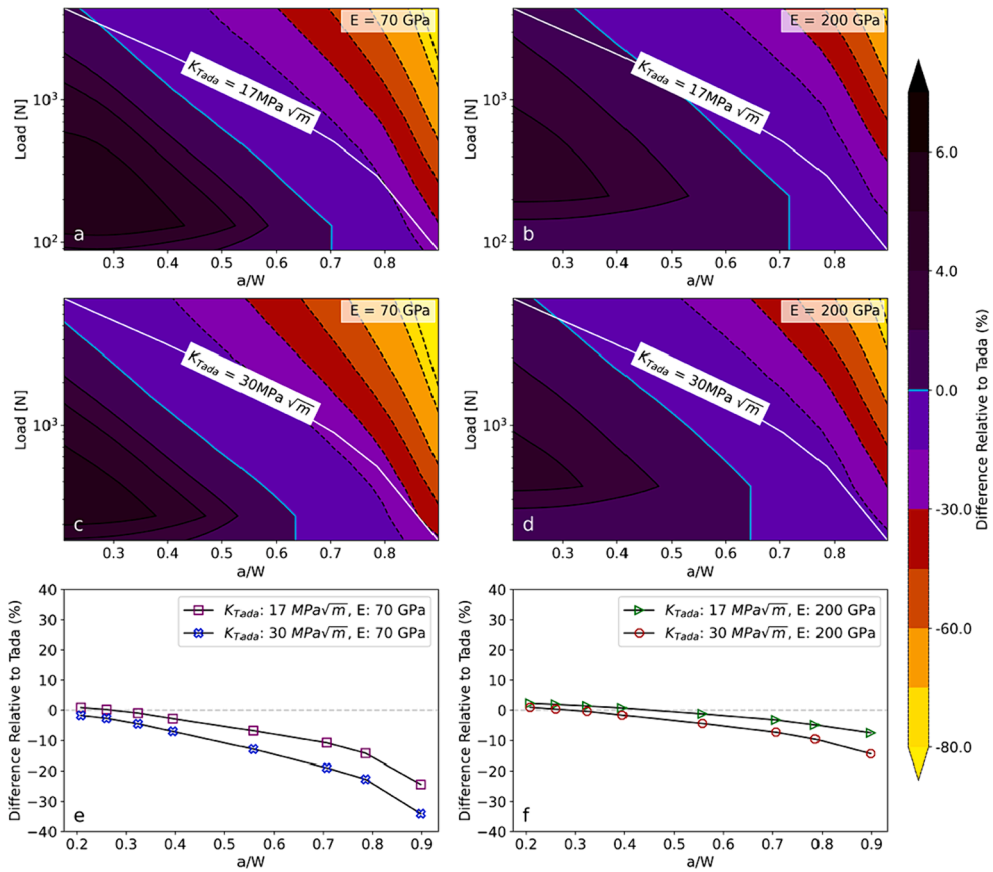
Fig. 11. Contours of the relative difference between K_{FE} from non-linear finite element analysis and K_{Tada} for the model based on the real SEN(T) geometry, as a function of a/W and load for the bounding material stiffness cases: Al (70 GPa, a and c) and Ni/Steel (200 GPa, b and d). The top row (a and b) corresponds to a $K_{Tada} = 17$ MPa $\sqrt{m}$, while the middle row (c and d) corresponds to a $K_{Tada} = 30$ MPa $\sqrt{m}$. The annotated white line shown in (a-d) represents the loads (predicted by Eq. 1) to maintain a constant driving force across a/W; the cyan dashed line in (a-d) represents a relative difference of zero for visual references. The corresponding relative difference along the annotated white lines are plotted in e and f. (For interpretation of the references to color in this figure legend, the reader is referred to the web version of this article.)

discussion is three-fold: (1) compare the results observed herein to those reported in the literature from both a computational and experimental perspective, (2) leverage both the current results and prior reports to identify the factors governing the observed discrepancies between Eq. 1 and the true K, and (3) comment on the implications of observed findings, particularly regarding the validity of extensive EAC and environment-sensitive fatigue crack propagation data developed using the SEN(T) specimen.

4.1. Comparison with literature FE results

Reports of geometrically non-linear finite element modeling of the elastic K for the SEN(T) specimen are limited to the work of Galyon Dorman and Fawaz, who modeled the pin-loaded SEN(T) configuration using the material properties of AA7056-T651, large H/W of 20, a/W of 0.5, and K_{Tada} of 17.1 MPa $\sqrt{m}$ [50]. The modeled K_{FE} from these calculations was 30 % lower than that expected from K_{Tada}, yielding a relative difference (Eq. 2) of -0.30. This reported deviation is significantly larger than was observed for the same material, geometry, and loading conditions in the current study (Fig. 10). Specifically, the current modeling exhibited a relative difference of -0.05 for AA7075-T651 at these a/W and K_{Tada} levels. In fact, even if a significantly higher K_{Tada} of 30 MPa $\sqrt{m}$ (which is the upper bound of experimental relevance for this alloy) is used in the calculations (Fig. 11), the observed difference at a/W = 0.5 only rises to -0.11, still well below the -0.3 reported by Galyon Dorman and Fawaz [50].

The origins of the difference between the two calculations cannot be rigorously explored since the full details finite element modeling conducted by Galyon Dorman and Fawaz were not reported [50]. However, examination of a separate final report [51] written by these authors reveals reduced disagreement with the current calculations. Specifically, this report contains K_{FE} results at 13 different a/W values (from both geometrically linear and non-linear calculations) for the same SEN(T) geometry and AA7075-T651 studied in the current manuscript. While the details of the modeling and the applied K_{Tada} were not provided, these additional calculations showed relative differences of $+0.005$ for $0.2 < a/W < 0.5$, -0.002 at a/W of 0.6, -0.01 at a/W of 0.7 and -0.04 at a/W of 0.8. Such results better align with the K = 17 MPa $\sqrt{m}$ results for AA7075-T651 in Fig. 11 for a/W < 0.4, but do not fully capture the

observed decrease in true K as a/W increases further. This suggests that a lower K_{Tada} than 17 MPa$\sqrt{m}$ was employed for these simulations by Galyon Dorman and Fawaz, underscoring the K dependence on the extent of disagreement between Eq. 1 and true K.

4.2. Compilation of fatigue crack growth rate data

Given the over 60 years of use for the pinned SEN(T) geometry [2], substantial fatigue crack growth rate data exist to augment and compare with the current experiments. These data are summarized in Table 3, which documents the material, environment, applied-maximum K_{Tada}, R, H/W (defined in Fig. 3), and observed-da/dN trend for programmed-constant ΔK_{Tada} loading per Eq. 1. For completeness, the current experiments from Figs. 6-8 are summarized in Rows 12 through 18.

The first two rows of Table 3 list the literature results that reported declining da/dN under programmed-constant ΔK_{Tada} loading, which include the studies of Wei and coworkers [47] as well as Galyon Dorman and Fawaz [50] that were summarized in depth in preceding sections. Rows 3 and 4 summarize the results of ~ 40 experiments performed by Galyon Dorman and Fawaz that broadly assessed the effect of fatigue protocol changes and crack closure retardation of da/dN for pinned SEN(T) specimens [51]. These results are notable as they reported steadily declining da/dN at programmed-constant $\Delta K_{Tada} = 6$ MPa$\sqrt{m}$ for all test conditions at R of 0.65 (Row 3), as well as for R of 0.8 and 0.1 (Row 4).

These reports of declining da/dN are contrasted by the historical studies performed by Gangloff and coworkers on both high strength steels and aluminum alloys, summarized in Rows 5–11 of Table 3. Considering the experiments performed on steels, the work reported in Row 5 revealed steady-constant da/dN for a 10-Ni steel with > 1 GPa yield strength at 12 different ΔK_{Tada} for a/W up to 0.3 and R = 0.1 [13]. Critically, the magnitude of each measured da/dN agreed with data collected from C(T) specimens of the same steel, as reported by $\simeq$20 laboratories participating in an ASTM test program [62]. These same nominal findings of steady-constant da/dN were also noted for the experiments described in Rows 6 and 7, which were performed on two high strength alloy steels in both H_2 and hydrocarbon gas-mixture environments at R = 0.1 from a/W of 0.01 to 0.1 [17].

Regarding Al alloys, Piascik and Gangloff noted constant da/dN for a/W of 0.02 to 0.35 for peak-aged AA2090 immersed in 1 %

Table 3
Summary of experimental da/dN changes during constant ΔK_{Tada} loading of pinned SEN(T) specimens.

#	Authors	Material	Environment	Maximum K_{Tada} (MPa$\sqrt{m}$)	R_{Tada}	H/W	a/W	Growth Rate Response @ Constant ΔK_{Tada}
1	Wan et al., 1996 [47]	AA2024-T3	Dry O_2	5.6 11.1	0.1	2	0.02 to 0.5	Steady decrease in da/dN by 20–40 %
2	Dorman-Fawaz, 2019 [50]	AA7075-T651	Ambient-Humid Air	17.2	0.65	29	0.1 to 0.6	Steady decrease in da/dN by 50 %
3	Dorman et al., 2016 (Figs. 56-69) [51]	AA7075-T651	Ambient-Humid Air	17.2	0.65	29	0.1 to 0.6	Steady decrease in da/dN by of order 50 % for 40 experiments following [19]
4	Dorman et al., 2016 [51]	AA7075-T651	Humid Air	6.7, 17.2, 30.0	0.1, 0.65, 0.8	29	0.1 to 0.55	Similar-steady decrease in da/dN by of order 50 %
5	Gangloff et al., 1992 [13]	10 Ni steel	Ambient Humid Air	5 to 40	0.1	~20	0.01 to 0.3	Constant da/dN at 12 levels of constant ΔK_{Tada}
6	Gangloff, 1988 [17]	4130 steel	UHV, H_2, $H_2 + C_xH_y$	19.6	0.1	~10	0.02 to 0.1	Constant da/dN at 4 different gas environments
7	Gangloff, 1988 [17]	4340 steel	UHV, H_2, $H_2 + C_xH_y$	16.7	0.1	~10	0.01 to 0.1	Constant da/dN at 4 different gas environments
8	Piascik-Gangloff, 1991 [18]	AA2090-T8	Aqueous NaCl	11 to 17	0.1 to 0.9	~20	0.02 to 0.35	Constant da/dN
9	Ciccone, 2005 [48]	AA7075-T6511	Aqueous LJSS	8.3	0.1	29	0.1 to 0.7	Constant da/dN
10	Ciccone, 2005 [48]	AA7055-T74511	Aqueous Modified LJSS	8.3	0.1	29	0.1 to 0.55	Steady decrease in da/dN by factor of 3
11	Ciccone, 2005 [48]	AA7055-T74511	Aqueous LJSS	8.3	0.1	29	0.1 to 0.87	Constant da/dN
12	Fig. 6a	CrNiMoV	Ambient-Humid Air	28.6	0.65	29	0.03 to 0.9	Constant da/dN; increase at a/W = 0.9
13	Fig. 6b	Custom 465-H900	Ambient-Humid Air	28.6	0.65	29	0.1 to 0.82	Constant da/dN; decrease at a/W > 0.65
14	Fig. 6c	316L	Ambient-Humid Air	23.3	0.7	29	0.14 to 0.74	Steady decrease in da/dN by 30 %
15	Fig. 6d	17-4PH H1025	Ambient-Humid Air	18	0.5	24	0.12 to 0.8	Constant da/dN; decrease at a/W > 0.7
16	Fig. 7a	AA7075-T651	Ambient-Humid Air	17.2	0.65	29	0.08 to 0.9	Constant da/dN; increased at a/W > 0.8
17	Fig. 7b	AA5456-H116	Ambient-Humid Air	10	0.5	14	0.1 to 0.80	Steady da/dN increase; decrease at a/W > 0.65
18	Fig. 8	Beta-C (ST/A)	Ambient-Humid Air	30	0.5	29	0.33 to 0.76	Sharp-continuous decrease in da/dN by factor of 10

NaCl solution at a fixed electrode potential for both low and high R (0.1 to 0.9) [18]. Similar results were also noted for peak-aged AA7075 by Ciccone, who performed constant ΔK_{Tada} experiments in an aqueous solution simulating that in the lap joint of an aging commercial aircraft and observed steady-constant da/dN for a/W from 0.1 to 0.7 and across multiple replicate SEN(T) specimens [48]. However, some variability was reported in these results, with particular dependence on the testing solution employed. For example, Ciccone reported declining da/dN for 7055-T74511 under constant ΔK_{Tada} loading in a modified lap joint simulated solution that promoted corrosion product formation. It was speculated in this study that this corrosion product was responsible for the observed decline via crack closure effects [48]. However, some variability (with isolated specimens exhibiting modest declines in da/dN) was also observed for testing on AA7075-T651 in unmodified lap joint simulated solution, shown in Fig. 12, which cannot be explained by corrosion product-induced closure.

In total, the compilation of data presented in Table 3 implies four general da/dN versus a/W trends during constant-programmed ΔK_{Tada} loading as prescribed by Eq. 1:

1. High strength, high modulus steels (Rows 5–8,12–13, 15 in Table 3) exhibit constant da/dN with increasing a/W over the tested ranges of ΔK_{Tada}, geometry, R, and a/W.
2. Steadily decreasing da/dN with increasing a/W was noted for moderate strength stainless steel (Row 14) and a high strength titanium alloy (Row 18), and Al alloys (Rows 1 to 4, 10).
3. Transition behavior where a constant da/dN changed to steadily declining da/dN for two steels above a critical a/W of 0.65 to 0.7 (Rows 13 and 15) as well as for two Al alloys above a critical a/W of 0.7 to 0.8 (Rows 16 and 17).
4. Variable behavior, where both constant da/dN as well as steadily decreasing da/dN with increasing a/W occurs for replicate experiments of a single alloy, environment and loading level (Rows 9 and 11 and Fig. 12).

Examination of these overarching trends in Table 3 imply that for a sub-set of experiments the actual K may have deviated below K_{Tada} (Eq. 1). The extent of this stress intensity error varied with a/W and alloy modulus of elasticity for pin-loaded SEN(T) geometries similar to that in Fig. 10. Since all crack lengths represented in Table 3, as well as in Figs. 6 to 8, were within the stated applicable range of a/W up to 0.95 for K_{Tada} [35], it is reasonable to conclude that the non-linear geometric effect alluded to by Srawley et al. [3], Dorman and Fawaz [50,51], and Wan et al. [47] could be causing this behavior. However, several factors acting either on their own or in concert could also contribute to this behavior, including: (1) experimental variability, (2) crack closure, (3) large-scale crack tip plasticity, and/or (4) the applied boundary conditions not aligning with those assumed for K_{Tada}. The role of each listed factor is assessed in ensuing sections.

4.3. Role of experimental variability and inter-laboratory differences

The majority of fatigue experiments in Table 3, including those from the present study, were performed with single SEN(T) specimens. Multiple fatigue crack growth experiments, conducted under nominally identical conditions, and employing a standardized specimen such at the C(T), typically lead to factors of 2 to 10 difference in da/dN at a given ΔK [62,64]. This expectation is affirmed by the da/dN versus a/W data for eight constant ΔK_{Tada} experiments on AA7075-T7651 in LJSS (Fig. 12), which demonstrate that crack growth rates from test-to-test differed by up to 1.5-fold from the population mean, ranging from $\sim 7x10^{-5}$ to $\sim 2.2x10^{-4}$ mm/cycle [48]. The data in Fig. 12 illustrate two classes of different da/dN versus a/W variations – those within a single experiment and from test-to-test – which are likely due to subtle differences in microstructure, residual stress, specimen alignment, dcPD instrumentation,
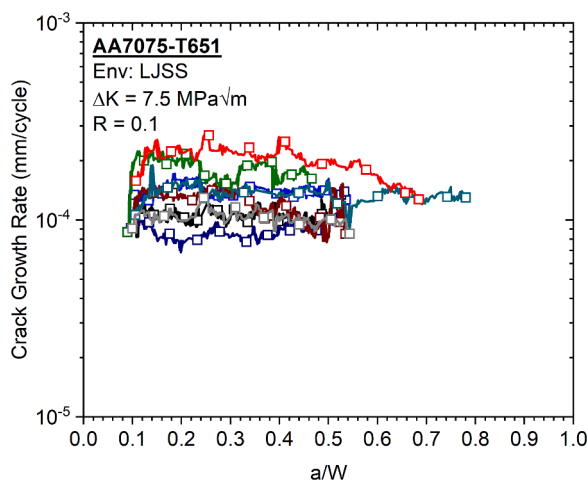

Fig. 12. Measured fatigue crack growth rate as a function of normalized crack length (a/W) for eight duplicate AA7075-T651 SEN(T) specimens immersed in lap joint simulated solution (LJSS) loaded at R = 0.1 and a constant Δ K = 7.5 MPa√m. Results extracted from Ciccone [48]. (For interpretation of the references to color in this figure legend, the reader is referred to the web version of this article).

environment and perhaps other factors. Similar test-to-test variability is also noted in the data from 40 constant-ΔK_{Tada} experiments (Table 3, Row 3) conducted by Galyon Dorman and Fawaz [51].

While test-to-test variations in measured da/dN are important for conservative structural life prognosis and management, trends of either constant or decreasing da/dN are not well explained by any aspect of the test method that would be associated with test-to-test variability. The results of the many SEN(T) experiments carried by Galyon Dorman and Fawaz [51] support this assessment, as these experiments resulted in similar steady-declining da/dN with increasing a/W despite systematic variations in test method, alloy, and specimen machining details. However, there are notable exceptions to this assertion. As shown in Fig. 12, replicate experiments with SEN(T) specimens of peak-aged AA7075-T651 [48] exhibited different da/dN versus a/W *trends*; the majority trend among eight-replicate tests was constant da/dN and the minority trend was steadily decreasing da/dN. Similarly, Galyon Dorman and Fawaz consistently reported steadily decreasing da/dN with rising a/W for AA7075-T651 (Table 3, Rows 3 and 4) [50,51], but Fig. 7 shows nominally constant da/dN for $0.08 < a/W < 0.8$, followed by a decline in da/dN for a/W above 0.8 for this same alloy, applied ΔK_{Tada}, and SEN(T) geometry/loading protocol.

The cause of these test-to-test variabilities in da/dN versus a/W *trends* (rather than da/dN magnitudes, as is often the focus) are not currently understood. While such behavior should certainly be explored further, a holistic assessment of the present results (Figs. 6 to 8) and the summarized literature data in Table 3 strongly suggests that test-to-test variability cannot explain why: (1) for some alloys and loading conditions, da/dN is truly constant with increasing a/W, while (2) for other conditions, steadily decreasing da/dN under constant-programmed ΔK_{Tada} is real. Factors that can cause such differences in behavior are now considered, particularly the role of alloy/loading specific crack closure, large-scale/net-section plasticity, and non-linear geometric changes.

4.4. Role of crack closure

Fatigue crack wake closure occurs when the upper and lower faces of the crack wake come into contact during unloading and due to one or more mechanisms [65,66]; this reduces the effective mechanical driving force for fatigue crack growth (ΔK) if contact occurs before the applied-minimum load is reached. For example, the use of an aqueous electrolyte in several experiments reported in Table 3 suggest that corrosion product and microstructure roughness-based mechanisms for closure could potentially be important. This arises from the fact that under constant ΔK loading, the applied minimum and maximum loads each decrease as a/W increases. If R is low, then the combination of a low applied force and continual reduction in force as a/W increases, as well as the time-dependent thickening of a reaction product, could result in the progressive onset/increase of closure and concomitant-steady decrease in the effective ΔK. This reduction in effective ΔK manifests as either a progressively worsening decline in da/dN as a/W increases, or a constant da/dN that begins to trend downward above a critical a/W (when closure begins to occur).

Concerns related to a potential effect of crack closure are amplified by the reality that crack closure is very challenging to measure for the conditions represented in Table 3. As such, effective values of ΔK_{Tada} versus a/W were not reported for any of the studies listed in Table 3, hindering direct quantification of the impact closure may be having. However, a holistic evaluation of Table 3 strongly suggests that closure is not an important cause of the observed reductions in measured da/dN. This view is justified by the fact that nearly all of the fatigue experiments used R values above 0.5, which typically limit closure effects. However, the most salient evidence for why the observed declining da/dN is unlikely due to crack closure is from the report of Galyon Dorman and Fawaz [51]. Specifically, for AA7075-T651 (Table 3, Row 4), continuously declining da/dN was observed in three experiments conducted at ΔK of 6.0 MPa$\sqrt{m}$ and R of 0.1, 0.65 and 0.8 [51]. In fact, the sharpest decline in da/dN was reported for the highest R of 0.8, which is opposite of expectations for a crack closure-driven behavior [66]. In addition to these fatigue experiment-based observations, it is also notable that similar reductions in applied K below K_{Tada} were also noted during the monotonic-loading compliance experiments conducted by Sullivan [2] as well as Srawley and coworkers [3]. Critically, such observations were noted under conditions where closure cannot
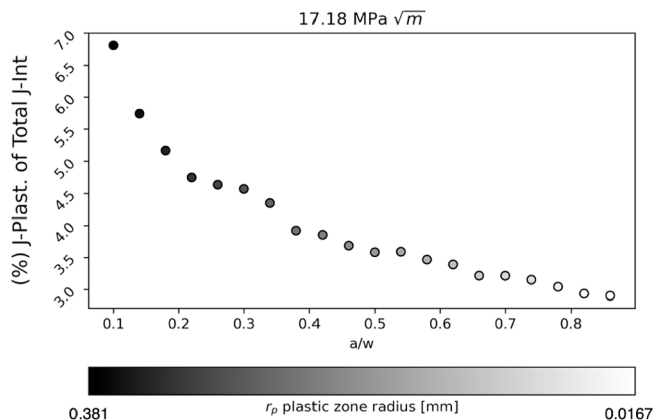

Fig. 13. Percent of J_P of total J-integral calculation from EPFM and LEFM as a function of normalized crack length for AA7075-T651 for constant $K_{Tada} = 17$ MPa$\sqrt{m}$. The maximum plastic zone radius referenced from measured from the crack tip is also included as a color bar. (For interpretation of the references to color in this figure legend, the reader is referred to the web version of this article.)

possibly impact the applied K, strongly suggesting that other factors are responsible.

4.5. Role of large-scale crack tip plasticity

A second factor that could cause da/dN to deviate from a constant value during constant ΔK_{Tada} loading is an a/W-dependent increase in the influence of plastic deformation on the crack tip field. If the applied load is sufficiently high, or the uncracked ligament is sufficiently small, then the assumptions of linear elastic fracture mechanics (LEFM) are no longer valid, resulting in increasing deviation between the real K and K_{Tada}. Given that many of the tested SEN(T) coupons listed in Table 3 have smaller width and thickness relative to other common specimen geometries (e.g., C(T) specimens [5]), it is possible that elastic–plastic fracture mechanics (EFPM) may be more applicable than Eq. 1. The fact that the observed declines in da/dN were mostly noted for the lowest strength steel and Al alloys in Table 3 supports an evaluation of the potential role of crack tip plasticity on the mechanical driving force.

To assess the possible contribution of crack tip plasticity, 3D finite element calculations of the calculated J as a function of a/W were performed under both linear elastic conditions (LEFM) and using the elasto-plastic (EPFM) material properties for AA7075-T651 [54]. The same geometry parameters and loading (maximum $K_{Tada} = 17$ MPa$\sqrt{m}$) as the experiment in Fig. 11a were employed for this calculation. For simplicity, only H/W = 29 was simulated, as it represented the largest deviation. Note that this analysis can only be qualitatively related to the reported fatigue crack growth kinetics since J is not rigorously applicable to fatigue loading due to the assumption of no unloading in the original J-integral derivation [67,68]. EPFM simulations decompose total J integral into plastic (J_p) and elastic (J_e) portions. The percentage of J_p is illustrated as a function of a/W in Fig. 13, and reveals two key observations. First, the effect of plasticity on the real K is not negligible at low a/W for the tested material, geometry, and loading combination. Contributions of J_p range from 7 % at a/W of 0.1 down to 3 % at an a/W of 0.9. This change is both realistic and expected since the size of the monotonic plastic zone decreases in radius from 0.381 mm to 0.0167 mm due to the decreasing K as the crack propagated when loading was applied per K_{Tada}. Second, some portion of J_p is present across the entirety of a/W. This finding leads to the question of if single parameter LEFM is valid or acceptable for this particular geometry and loading condition. Additionally, the change in driving force due to plasticity follows the general trend (at a lesser magnitude) of the declining da/dN with increasing a/W behavior noted for the experiments summarized in Table 3. This suggests that plasticity may contribute to the declining da/dN, but additional studies are needed to quantify what values of K and load would be affected.

4.6. Role of non-linear boundary condition change

The current finite element calculations presented in Figs. 10 and 11 provide an opportunity for new insights on what is inducing the falling da/dN for constant-applied ΔK_{Tada} loading. Specifically, these results establish that the computational methods used to derive K_{Tada} (Eq. 1) do not accurately describe the evolving boundary conditions for the pinned SEN(T) geometry over the a/W range up to 0.95 [35]. Note that this possibility has been previously reported by several authors. For example, it was argued that K_{Tada} does not accurately account for the changing-load eccentricity induced by the pinned SEN(T) yawing forward as the crack progresses [3,39,46,47]. Gross et al. speculated that this effect was responsible for the difference between linear boundary collocation calculations and compliance measurements on pinned SEN(T) specimens of AA7075-T6 [3,39]. Wan et al. proposed that the moment induced by such yawing, as well as a potential role of pin friction, as suggested originally by Pook [46], were responsible for decreasing da/dN vs. a/W during fatigue testing of AA2024-T3 SEN(T) specimens [47]. Others proposed that K_{Tada} does not account for the impact of geometry parameters (like H/W) known to affect other SEN(T) K solutions that are sensitive to changes in loading-boundary conditions [6,69]. For example, Dorman and Fawaz claimed that the large-effective H/W of the AA7075-T651 pinned SEN(T) specimen and loading configuration caused declining da/dN during constant ΔK_{Tada} loading [50].

This literature suggesting that K_{Tada} is inaccurate due to improper boundary conditions is inconsistent with experiments from both the current and prior studies (summarized in Table 3). In particular, fixed ΔK_{Tada} experiments on seven high and ultra-high strength steels, as well as several high strength Al alloys all exhibited nominally constant da/dN over a broad range of a/W. Such fatigue-based results were augmented by the monotonic photoelasticity experiments of Sanford and Kirk on polycarbonate [40], which also exhibited good agreement with K_{Tada}. However, the current study also observed declining da/dN versus a/W relationships for Beta-C titanium (Fig. 8) and 316L stainless steel (Fig. 6c), consistent with the prior work suggesting errors in K_{Tada}. This dichotomy of experimental results, and the soundness of the many experiments represented in Table 3, therefore suggest a complex linkage between applied load, material, and sample geometry that is not adequately captured by K_{Tada}. Comparison of the linear and non-linear geometric finite element calculations in Fig. 10 confirms this assessment. Specifically, the linear-geometric finite element calculations revealed good agreement with K_{Tada} for a range of applied forces and H/W. Such results are expected given (1) that this method was used by Tada to create this K solution [35] and (2) other studies using linear-geometric finite element calculations previously validated K_{Tada} [6,36–38]. Conversely, based on higher-order, non-linear geometric finite element calculations, K can clearly deviate below K_{Tada}, with the occurence and amount dependent on applied load, a/W, geometry, and material stiffness, as demonstrated by Figs. 10 and 11.

The difference between the geometrically linear and non-linear finite element results arises because the linear geometry assumption over-predicts the extent of yawing for the pinned SEN(T) geometry. This results in an under-prediction of the force necessary to achieve K_{Tada} for a given geometry and crack length, thus the calculated K_{Tada} from Eq. 1 is larger than the actual applied K. Moreover, since progressively larger displacements occur as the pinned SEN(T) increasingly yaws, this over-prediction of the applied K from linear-geometry FE becomes increasingly significant and motivates the need for a geometrically non-linear approach. However, the use of non-linear finite element analysis increases the sensitivity to factors such as the moment arm length (i.e., H/W),

applied load, load train stiffness, and material stiffness. Specifically, the non-linear geometry effect on the accuracy of K_{Tada} would be expected to increase as alloy-elastic modulus decreases, a/W increases, and/or applied load increases. Such effects are, in all cases, captured by the modeling presented in Figs. 10 and 11, which confirmed the reduction in real crack tip K below the assumed applied K_{Tada} with decreasing modulus, increasing a/W, and increasing load. However, important differences were observed to be correlated with different material families, therefore the model predictions are best assessed by considering the fatigue data in Table 3, categorized by alloy stiffness.

4.6.1. Steels

All fatigue experiments conducted on six different compositions of high and ultra-high strength steel (summarized in Table 3) showed effectively constant da/dN with increasing a/W at constant-applied ΔK_{Tada} when a/W was less than 0.6. Constant da/dN in this regime is apparent in the published data [13,17,49] and the current experiments (Fig. 6). This general observation is well-explained by the modeling shown in Fig. 11. First, the maximum K_{Tada} during this fatigue experiments was always less than 30 MPa$\sqrt{m}$ and often ~ 20 MPa$\sqrt{m}$. Examination of Fig. 11 demonstrates that the expected reduction in the true applied K relative to the assumed K_{Tada} for steels at a/W < 0.6 is less than −5% at 30 MPa$\sqrt{m}$ and −2% at 20 MPa$\sqrt{m}$. Such a reduction in K is sufficiently small that a tangible reduction in da/dN is unlikely to be observed, consistent with the noted constant da/dN versus a/W relationship for each high modulus steel. Second, the non-linear calculations in Fig. 11 indicate that beyond a/W = 0.6, a steep reduction in the true applied K relative to the assumed K_{Tada} occurs, with the difference reaching between −5 to −15 %, depending on the applied load and a/W. Such behavior is consistent with results in Fig. 6b and 6d where, at fixed ΔK_{Tada}, da/dN decreases from the constant plateau when a/W exceeds 0.65 to 0.7 for 17-4PH and Custom 465 stainless steels. Interestingly, this falloff in da/dN at large a/W was not observed for the experiment on CrNiMoV (Fig. 6a), where constant da/dN persists for a/W up to ~ 0.9. Speculatively, the small increase in the total-K driving force due to increasing non-zero J_p contribution (on the order of 3 % expected based on Fig. 13) for these small uncracked-ligament sizes may offset the fall in crack tip driving force due to the non-linear boundary condition shift.

The lowest strength steel examined, 316L stainless steel, exhibited a steadily declining da/dN (reaching nearly 30 % reduction) when stressed at constant ΔK_{Tada}, which began at small a/W (Fig. 6c). Such a result was surprising given that the applied maximum K_{Tada} for this experiment (~23 MPa$\sqrt{m}$) was notably less than that used (~28.5 MPa$\sqrt{m}$) during the testing on the other steels shown in Fig. 6. It is speculated that this result may be due to the proximity of the employed ΔK_{Tada} to the near-threshold regime for fatigue crack growth in 316L. For example, a 3 % reduction in ΔK from Eq. 1 would have significantly more impact as cracking moves from the Paris regime with a ΔK^3 dependence ($1.03^3 = 1.09$) to the near-threshold regime with a ΔK^8 dependence ($1.03^8 = 1.27$). Alternately, this behavior could be due to a residual stress distribution produced by the cold work used to manufacture this non-heat treated steel, in contrast to the higher strength quenched and tempered martensitic steels. Such residual stress could act to reduce the crack tip K further below both the assumed applied K_{Tada} and non-linear K_{FE}. An experiment with stress relieved 316L stainless steel as well as replication of the single test result shown in Fig. 6c and exploration of other ΔK levels are needed to clarify this unexpected behavior.

4.6.2. Aluminum alloys

For lower elastic modulus aluminum alloys, the non-linear FE results in Fig. 10 suggest a stronger decrease in the true applied K for a given assumed K_{Tada} compared to steel, and thus a stronger reduction in linear da/dN as a/W increases. For example, at a/W of 0.6, the non-linear K_{FE} is 7 % and 14 % less than K_{Tada} for applied K_{Tada} of 17 MPa$\sqrt{m}$ and 30 MPa$\sqrt{m}$, respectively. This stronger non-linear influence is consistent with the fact that reduced da/dN was first reported as a problem for SEN(T) specimens of AA2024 and AA7075 (Table 3, Rows 1–4). Indeed, these 20 % to 50 % reductions in da/dN are consistent with a 7 % reduction of ΔK_{Tada} and the conventional da/dN dependence of ΔK^{3-6} ($1.07^{3-6} = 1.2$ to 1.5) for the Paris region.

While the experimental fatigue data in Table 3 for Al alloys generally support the predictions of the magnitude of non-linear boundary condition change effects on K_{Tada}, confirmation is somewhat ambiguous. For example, Ciccone did not observe a systematic da/dN reduction for AA7075-T651 (Table 3, Row 9) [48], while reductions in da/dN were observed for this alloy by Galyon Dorman and Fawaz [50]. This difference could be reasonably ascribed to the fact that Dorman and Fawaz consistently applied a higher K_{max} (17.2 MPa$\sqrt{m}$) compared to Ciccone (8.3 MPa$\sqrt{m}$), thus supporting the non-linear FE prediction of a load-level effect (Fig. 10) and falling da/dN. Yet, this same K_{max} was used for testing in the current effort (Fig. 7a) on the same alloy and was not observed to induce a sustained decline in da/dN. Such ambiguity is further underscored by the results of Ciccone on AA7055-T7451 [48], where samples tested under constant ΔK_{Tada} loading either exhibited declining or constant da/dN, and that of Piascik and Gangloff on AA2090 (Table 3, Row 8), who observed constant da/dN for a wide range of applied-constant ΔK_{Tada} and K_{max}, albeit over a limited a/W window up to 0.35 [18]. While the sum of the experimental and computational work support an increased error in K_{Tada} for aluminum alloys, this strong variation in the magnitude of the non-linear geometry effect from study-to-study (or even within a single study) merits further exploration to understand the source of these ambiguities.

4.6.3. Titanium alloys

Titanium alloys of intermediate-elastic modulus (~100 GPa) compared to steel and Al alloys should exhibit reductions of K_{Tada} intermediate to those modeled in Fig. 10. While only a single SEN(T)-based fatigue experiment is available for high strength (body-centered cubic) titanium alloys, this result (Fig. 8) revealed that da/dN at constant ΔK_{Tada} ($K_{max} = 30$ MPa$\sqrt{m}$) decreases by an order of magnitude as a/W rises from 0.3 to 0.75. This decrease is much larger than those observed for steels and Al alloys (Table 3) and is much greater than expected based on the non-linear FE results in Fig. 10. The cause of this strong reduction in da/dN is not fully understood, but is notable that a significant portion of the decrease in da/dN occurs over a/W from 0.65 to 0.75, consistent with the onset of sharply increasing error in applied K reported in Fig. 10. Speculatively, the reduction in true applied K may be sufficiently

large that the near-threshold regime is being approached (resulting in a sharper decline in da/dN), but additional experiments are necessary to confirm this possibility. However, the pinned SEN(T) specimen was successfully used to characterize the da/dN behavior of Ti-6 V-4Al, so long as a/W < 0.6, paralleling the details considered in the next section for Ni-based superalloys [70].

4.6.4. Ni-based superalloys

Since Ni-based superalloys exhibit elastic moduli similar to steel, this class of alloys should exhibit small reductions in the true crack tip K, compared to K_{Tada}. However, to the authors' knowledge, there are no published data of da/dN versus a/W at programmed-constant ΔK_{Tada} for pinned SEN(T) specimens to test this expectation. That being said, Van Stone and coworkers successfully applied the small pin-loaded SEN(T) specimen with programmed-declining ΔK_{Tada} to establish da/dN in the near threshold regime for high strength Ni superalloys (e.g., Rene 95 and PWA 1484) [24,25]. Note that these specimens were small; thickness = 2.5 mm, W = 10 mm and H/W = 6.5 [70]. At threshold crack 'arrest', the applied load range was fixed at a somewhat higher value and ΔK_{Tada} increased with subsequent crack growth to a maximum K_{Tada} of 40–55 MPa$\sqrt{m}$. Measured da/dN values were well aligned with extensive data obtained from surface crack specimens that were optimized for accuracy [13,24,25]. Unpublished-proprietary studies with a variety of Ni superalloys used the SEN(T) and Eq.1 to produce da/dN data that agreed with surface-crack growth rates so long as the SEN(T) a/W was < 0.6 and net section stress (simply load/uncracked ligament area) was < 75 % of alloy yield strength [70]. Fig. 10 shows that K from the 3-D geometrically non-linear FE model is only 4–5 % less than K_{Tada} for applied K of 30 MPa$\sqrt{m}$ and an alloy modulus of 200 GPa, with very large H/W of 23. Smaller differences, extending to higher a/W or higher K_{Tada}, are predicted for H/W of 6–8. As such, these FE model predictions are consistent with this laboratory experience for Ni-based alloys, which further affirms the validity and broad applicability of K_{Tada} given by Eq. 1 for the alloy, a/W, H/W and stress intensity bounds given by the non-linear FE results in Figs. 9 and 10.

4.6.5. Other comparisons with experiments

Compliance and photo elastic measurements of the SEN(T) geometry are limited; however, those reported are consistent with the non-linear FE assessment of reductions from K_{Tada} represented in Figs. 9 and 10. The influence of load magnitude explains why Sanford and Kirk [40] observed excellent agreement between experimentally determined K and K_{Tada} for the SEN(T) specimen, despite using a compliant material (polycarbonate) for their experiments. While the exact loading conditions were not reported, the low toughness of polycarbonate (<5 MPa$\sqrt{m}$) would necessitate these authors to employ a low K in their photoelastic experiments. Decreasing H/W reduces the non-linear geometric influence on K. This explains why the compliance measurements of Srawley et al. [3] on AA7075-T6 (H/W of ~ 3.3), presented in Fig. 1b, reasonably agree with K_{Tada} over the same range of a/W where the calculations in Fig. 10a (H/W = 29) reveal increasing relative difference due to specimen yawing.

4.7. Implications and suggested future research directions

There are two overarching implications from the current study. First, comparison of experiment and modeling establishes that the K_{Tada} solution for the pinned SEN(T) geometry (Eq. 1) loses high accuracy only for specific combinations of specimen geometry, material stiffness, and applied loading. Potential error in K_{Tada} was suggested by others due to changing boundary condition and loading eccentricity during crack growth, but the effects were not quantified in those studies [47,50]. The current study demonstrates that the reduction of applied K compared to K_{Tada} arises from a complex non-linear geometry influence, and defines regimes of alloy stiffness, load, and uncracked ligament size where these errors become significant. This finding contrasts with the stated broad accuracy of K_{Tada} 0.05 < a/W < 0.95 [35–38,40]. However, these prior studies did not capture non-linear geometry effects. For example, the experimental validation by Sanford and Kirk utilized very low K loading [40], while modeling of Joyce and others used geometrically linear finite element approaches [34,36,37], which inherently neglect such effects.

As called for by others [47,50], it is necessary to develop a new K solution that can be broadly employed for pinned SEN(T) samples of different alloy stiffness and loading configuration by accounting for the influence of non-linear geometry change. Recently developed machine learning-based, genetic programming algorithms [71] were shown to be effective for developing straight-forward K solutions that accurately capture complex dependencies; such approaches can be leveraged for the pinned SEN(T). Moreover, geometrically non-linear FE modeling should be employed to assess the extent to which boundary condition changes affect accepted K solutions for other bending-based specimens such as the C(T) and eccentrically loaded single edge notch tension (ESE(T)) geometries employed in fatigue and EAC studies [72].

The second implication of this study is that there are clear combinations of material stiffness, specimen geometry, and loading that result in true K values that agree within 5 % or better with K_{Tada}. For example, the non-linear finite element simulations show that K_{Tada} is within 5 % of the calculated K value up to a/W = 0.6 for a realistic pinned SEN(T) specimen configuration (H/W = 29) loaded to K_{max} = 17 MPa$\sqrt{m}$ for Al alloys (Fig. 10). For stiffer steels, this critical a/W is 0.75 for this K level and 0.6 for higher K of 30 MPa$\sqrt{m}$. Nickel-based superalloys will likely align with this regime of validity established for steel, while Ti alloys will be intermediate to steel and Al alloys. This assessment is affirmed by the extensive fatigue crack growth data sets summarized in Table 3 and the compliance results of Srawley and Gross (Fig. 1b) [3,39].

The present results strongly support the conclusion that historical fatigue and EAC data developed using pinned SEN(T) specimens are overwhelmingly valid [13,17–21,26,27,48,52–55,61,62,73–83]. Nearly all these experiments were performed at a/W < 0.4, with many conducted at a/W of 0.1 or less, where non-linear geometry effects are minimal. Moreover, the threshold stress intensity (K_{TH}) where EAC initiates is generally < 20 MPa$\sqrt{m}$ for nickel alloys/steels and < 10 MPa$\sqrt{m}$ for Al alloys, leaving an appreciable range over which K_{Tada} and therefore measured crack growth rate (da/dt) vs. K relationships are valid. Nonetheless, it is likely that non-

negligible errors are present in the high-K_{Tada} portion of those SEN(T)-based datasets that exceed ~ 80 MPa$\sqrt{m}$ for high modulus steels and Ni alloys[28,75,76,79]; additional studies are needed to quantify the error in applied K for these experiments. As suggested by Fig. 13, large scale plasticity elevates the true crack tip K above the elastic K_{Tada} and K_{FE}. This contribution may be important for such high K levels and lower-strength alloys.

Future work should focus on understanding these effects for existing datasets, but also more generally on defining the expected error across the entire range of geometry, load, and material combinations for scenarios where using K_{Tada} is required (as may be the case for preprogramed control software systems). Such information could then be used to modify the specimen geometry design to maximize the usable a/W where K_{Tada} remains valid. Conversely, if a certain test geometry is dictated by material availability or other reasons, then (1) non-linear finite element simulations can be performed to determine the validity bounds of K_{Tada} for that specific geometry and/or (2) an experimental validation (akin to data in Figs. 6-8) could be conducted to explore the maximum a/W that results in constant growth kinetics.

5. Conclusions

The efficacy of the elastic solution for K_{Tada} for the pinned-rotating SEN(T) geometry was assessed via a combined approach that leveraged extensive-constant ΔK fatigue experiments and targeted finite element modeling simulations. From these data, the following conclusions are established:

Depending on the combination of the pin-loaded SEN(T) geometry (particularly H/W), alloy modulus, uncracked ligament size, and applied stress intensity, constant ΔK_{Tada} experiments exhibit either broadly constant, progressively decreasing, or constant-to-decreasing forms of da/dN vs. a/W at constant-applied ΔK_{Tada}.

These experimental trends suggest that the true K for the pinned SEN(T) geometry either equals or is less than K_{Tada}; this deviation is not constant and increases with those factors that promote increasing 'yawing' changes in the geometric boundary conditions of the SEN(T).

The existing solution for K_{Tada} was reproduced for a wide range of a/W, consistent with previous models, if linear geometric simulations are performed with constant boundary conditions. However, 3-D non-linear geometric finite element analysis establishes significant deviations from K_{Tada}.

Non-linear finite element modeling shows that yawing open inherent to the pinned SEN(T) geometry causes the true K to increasingly deviate below K_{Tada} as crack length increases, but only above a critical a/W. Modeling confirms that the amount of reduction increases with increasing pin spacing, decreasing uncracked ligament size, decreasing alloy stiffness, and increasing load for large H/W loading.

Experimentally observed reductions in measured da/dN at constant ΔK_{Tada} cannot be convincingly attributed to crack-wake closure or crack tip plasticity. Rather, occurrences of constant as well as declining and transition da/dN vs. a/W at constant ΔK_{Tada} are most consistently explained by the non-linear geometry influence not accounted for in K_{Tada}.

Most existing fatigue and EAC datasets based on pinned SEN(T) specimens are accurate because test conditions reside in regions of a/W, alloy stiffness, and applied loading where the true K is reasonably described by K_{Tada} (e.g., at critical a/W < 0.6 to 0.75 for Al alloys and steels, respectively, at relevant applied K). However, experimental cracking data collected at high K_{Tada}, or at larger a/W, will require non-linear FE correction of K_{Tada}.

A K solution should be developed for the pinned SEN(T) geometry to replace K_{Tada} that incorporates this influence of non-linear geometry effects, such as H/W.

CRediT authorship contribution statement

Zachary D. Harris: Writing – original draft, Methodology, Investigation, Conceptualization. **Joseph W. Cochran:** Writing – original draft, Methodology, Investigation. **Richard P. Gangloff:** Writing – review & editing. **Jacob D. Hochhalter:** Writing – review & editing, Supervision, Methodology, Conceptualization. **James T. Burns:** Writing – review & editing, Supervision, Funding acquisition, Conceptualization.

Declaration of competing interest

The authors declare that they have no known competing financial interests or personal relationships that could have appeared to influence the work reported in this paper.

Data availability

Data will be made available on request.

Acknowledgements

References

[1] Srawley JE, Brown W. Fracture Toughness Testing Methods. Fracture Toughness Testing and its Applications. West Conshohocken, PA: ASTM International; 1965. p. 133–98.

[2] Sullivan AM. New specimen design for plane-strain fracture toughness tests. Mater. Res. Stand. 1964;4:20–4.

[3] Srawley JE, Jones MH, Gross B. NASA TN D-2396: Experimental determination of the dependence of crack extension force on crack length for a single-edge notch tension specimen. 1964.

[4] ASTM E399-20: Standard Test Method for Linear-Elastic Plane-Strain Fracture Toughness of Metallic Materials. West Conshohocken, PA: ASTM International; 2020.

[5] ASTM E1820-20: Standard Test Method for Measurement of Fracture Toughness. West Conshohocken, PA: ASTM International; 2020.

[6] Zhu XK, Joyce JA. Review of fracture toughness (G, K, J, CTOD, CTOA) testing and standardization. Eng. Fract. Mech. 2012;85:1–46. https://doi.org/10.1016/j.engfracmech.2012.02.001.

[7] Dadfarnia M, Sofronis P, Somerday BP, Balch DK, Schembri P, Melcher R. On the environmental similitude for fracture in the SENT specimen and a cracked hydrogen gas pipeline. Eng. Fract. Mech. 2011;78:2429–38. https://doi.org/10.1016/j.engfracmech.2011.06.002.

[8] Zhu XK. Progress in development of fracture toughness test methods for SENT specimens. Int. J. Press. Vessel. Pip. 2017;156:40–58. https://doi.org/10.1016/j.ijpvp.2017.07.004.

[9] Zhu XK. Review of fracture toughness test methods for ductile materials in low-constraint conditions. Int. J. Press. Vessel. Pip. 2016;139–140:173–83. https://doi.org/10.1016/j.ijpvp.2016.02.006.

[10] Johnson HH. Calibrating the electric potential method for studying slow crack growth. Mater. Res. Stand. 1965;5:442–5.

[11] Schwalbe K-H, Hellmann D. Application of the electrical potential method to crack length measurements using Johnson's formula. J Test Eval 1981;9:218–21.

[12] Donald JK, Ruschau J. Direct current potential difference fatigue crack measurement techniques. In: Marsh KJ, Smith RA, Ritchie RO, editors. Fatigue Crack Measurement: Techniques and Applications. EMAS; 1991. p. 11–37.

[13] Gangloff RP, Slavik DC, Piascik RS, Van Stone RH. Direct current electrical potential measurement of the growth of small cracks. In: Larsen JM, Allison JE, editors. Small-Crack Test Methods, ASTM STP 1149. Philadelphia: American Society for Testing and Materials; 1992. p. 116–68.

[14] Ritchie RO, Lankford J, editors. Small Fatigue Cracks. TMS-AIME: Warrendale, PA; 1986.

[15] Gangloff RP, Ritchie RO. Environmental effects novel to the propagation of short fatigue cracks". In: Bilby BA, Miller KJ, Willis JR, editors. Fundamentals of Deformation and Fracture. Cambridge, UK: Cambridge University Press; 1986. p. 529–58.

[16] Gangloff RP. Crack size effects on the chemical driving force for aqueous corrosion fatigue. Metall. Trans. A 1985;16:953–69. https://doi.org/10.1007/BF02814848.

[17] Gangloff RP. Ethylene inhibition of gaseous hydrogen embrittlement in high strength steel. ASTM STP 924: Basic Questions in Fatigue 1988;Volume 2:230–51.

[18] Piascik RS, Gangloff RP. Environmental fatigue of an Al-Li-Cu alloy: part I. Intrinsic crack propagation kinetics in hydrogenous environments. Metall. Trans. A 1991;22:2415–28. https://doi.org/10.1007/BF02665008.

[19] Warner JS, Gangloff RP. Molybdate inhibition of corrosion fatigue crack propagation in precipitation hardened Al-Cu-Li. Corros Sci 2012;62:11–21. https://doi.org/10.1016/j.corsci.2012.03.038.

[20] Warner JS, Kim S, Gangloff RP. Molybdate inhibition of environmental fatigue crack propagation in Al-Zn-Mg-Cu. Int. J. Fatigue 2009;31:1952–65.

[21] Warner JS, Gangloff RP. Alloy induced inhibition of fatigue crack growth in age-hardenable Al–Cu Alloys. Int. J. Fatigue 2012;42:35–44. https://doi.org/10.1016/j.ijfatigue.2011.04.013.

[22] Bray GH, Glazov M, Rioja RJ, Li D, Gangloff RP. Effect of artificial aging on the fatigue crack propagation resistance of 2000 series aluminum alloys. Int. J. Fatigue 2001;23:265–76. https://doi.org/10.1016/S0142-1123(01)00159-1.

[23] Burns JT, Bush RW, Ai JH, Jones JL, Lee Y, Gangloff RP. Effect of water vapor pressure on fatigue crack growth in Al–Zn–Cu–Mg over wide-range stress intensity factor loading. Eng. Fract. Mech. 2015;137:34–55. https://doi.org/10.1016/j.engfracmech.2014.11.009.

[24] Van Stone RH. Residual life prediction methods for gas turbine components. Mater. Sci. Engng. A 1988;103:49–61. https://doi.org/10.1016/0025-5416(88)90551-4.

[25] Gallagher J, Nicholas T, Gunderson A, Ruschau J, Miedlar P, Hutson A, et al. AFRL-ML-WP-TR-2005-4102: Advanced High Cycle Fatigue Life Assurance Methodologies", . Dayton, OH: 2004.

[26] Crane CB, Gangloff RP. Stress corrosion cracking of Al-Mg alloy 5083 sensitized at low temperature. Corrosion 2016;72:221–41. https://doi.org/10.5006/1766.

[27] Pioszak GL, Gangloff RP. Hydrogen environment assisted cracking of a modern ultra-high strength martensitic stainless steel. Corrosion 2017;73:1132–56. https://doi.org/10.5006/2437.

[28] Gangloff RP, Ha HM, Burns JT, Scully JR. Measurement and modeling of hydrogen environment-assisted cracking in monel K-500. Metall. Mater. Trans. A 2014;45:3814–34. https://doi.org/10.1007/s11661-014-2324-z.

[29] Gangloff RP, Turnbull A. Crack electrochemistry modeling and fracture mechanics measurement of the hydrogen embrittlement threshold. In: Jones RH, Gerberich WW, editors. Modeling Environmental Effects on Crack Initiation and Propagation. Warrendale, PA: TMS-AIME; 1986. p. 55–81.

[30] Gangloff RP. Probabilistic fracture mechanics simulation of stress corrosion cracking using accelerated laboratory testing and multi-scale modeling. Corrosion 2016;72:862–80. https://doi.org/10.5006/1920.

[31] Saxena A, Bassi F, Nibur K, Newman JC. On single-edge-crack tension specimens for tension-compression fatigue crack growth testing. Eng. Fract. Mech. 2017;176:343–50. https://doi.org/10.1016/j.engfracmech.2017.03.030.

[32] Narasimhachary SB, Bhachu KS, Shinde SR, Gravett PW, Newman JC. A single edge notch specimen for fatigue, creep-fatigue and thermo-mechanical fatigue crack growth testing. Eng. Fract. Mech. 2018;199:760–72. https://doi.org/10.1016/j.engfracmech.2017.08.011.

[33] Zhu XK. Full-range stress intensity factor solutions for clamped SENT specimens. Int. J. Press. Vessel. Pip. 2017;149:1–13. https://doi.org/10.1016/j.ijpvp.2016.11.004.

[34] Slavik DC. Environmental Fatigue Crack Growth and Microscopic Damage Mechanisms in AA2090. University of Virginia; 1993. Ph.D. Dissertation.

[35] Tada H, Paris P, Irwin G. The Stress Analysis of Cracks Handbook. St. Louis, MO: Paris Productions Incorporated; 1985.

[36] Tokuda N, Yamamoto Y. Accurate determination of stress intensity factors in cracked plates. J. Soc. Naval Archit. Japan 1972;132:349–60. https://doi.org/10.2534/jjasnaoe1968.1972.132_349.

[37] Joyce J, Hackett E, Roe C. Effects of crack depth and mode of loading on the J-R curve behavior of a high-strength steel. In: Hackett EM, Schwalbe K–H, Dodds RH, editors. Constraint Effects in Fracture. West Conshohocken, PA: ASTM International; 1993. p. 239–63. https://doi.org/10.1520/STP18031S.

[38] Hammond MJ, Fawaz SA. Stress intensity factors of various size single edge-cracked tension specimens: A review and new solutions. Eng. Fract Mech. 2016;153:25–34. https://doi.org/10.1016/j.engfracmech.2015.12.022.

[39] Gross B, Srawley JE, Brown Jr. WF. NASA TN D-2395: Stress intensity factors for a single-edge-notch tension specimen by boundary collocation of a stress function. 1964.

[40] Sanford RJ, Kirk MT. A comparison of boundary and global collocation solutions for K and CMOD calibration functions. Exp. Mech. 1991;31:52–9. https://doi.org/10.1007/BF02325724.

[41] Wang W-C, Chen T-L. Half-fringe photoelastic determination of opening mode stress intensity factor for edge cracked strips. Eng. Fract. Mech. 1989;32:111–22.

[42] Bowie OL. Rectangular tensile sheet with symmetric edge cracks. J. Appl. Mech. 1964;32:208–12. https://doi.org/10.1115/1.3629588.

[43] Bowie OL, Neal DM. Single edge cracks in rectangular tensile sheet. J. Appl. Mech. 1965;32:708–9. https://doi.org/10.1115/1.3627290.

[44] Emery AF, Walker Jr GE, Williams JA. A Green's function for the stress-intensity factors of edge cracks and its application to thermal stresses. J. Basic Engng. 1969;91:618–24.

[45] Jack AR. Stress intensity factors for an edge notched tension specimen with restrained ends. Eng. Fract. Mech. 1971;3:349–50.

[46] Pook LP. The effect of friction on pin jointed single edge notch fracture toughness test specimens. Int. J. Fract. Mech. 1968;4:295–7. https://doi.org/10.1007/BF00185265.

[47] Wan KC, Chen GS, Gao M, Wei RP. On the conventional K calibration equations for single-edge-cracked tension specimens. Eng. Fract. Mech. 1996;54:301–5. https://doi.org/10.1016/0013-7944(95)00185-9.

[48] Ciccone MP. The Effect of Corrosion Product Formation on Fatigue Crack Closure of AA7075-T6511 and AA7055-T74511. University of Virginia; 2005.

[49] Thomas RLS, Scully JR, Gangloff RP. Internal hydrogen embrittlement of ultrahigh-strength AERMET 100 steel. Metall. Mater. Trans. A 2003;34:327–44. https://doi.org/10.1007/s11661-003-0334-3.

[50] Galyon Dorman SE, Fawaz SA. Examination of the effects of specimen geometry on single edge-cracked tension specimens. Eng. Fract. Mech. 2019;209:221–7. https://doi.org/10.1016/j.engfracmech.2019.01.028.

[51] Galyon Dorman SE, Rausch JW, Arunachalam SR, Burns JT, Gangloff RP, Fawaz SA. SAFE-RPT-16-045: Managing Environmental Impacts on Time-Cycle Dependent Structural Integrity of High Performance DoD Alloys. CO: Colorado Springs; 2016.

[52] Shoemaker TK, Harris ZD, Burns JT. Comparing stress corrosion cracking behavior of additively manufactured and wrought 17–4PH stainless steel. Corrosion 2022;78:528–46. https://doi.org/10.5006/4064.

[53] Pioszak GL, Gangloff RP. Hydrogen environment assisted cracking of modern ultra-high strength martensitic steels. Metall Mater Trans A Phys Metall Mater Sci 2017;48:4025–45. https://doi.org/10.1007/s11661-017-4156-0.

[54] Harris ZD, Burns JT. The effect of loading rate on the environment-assisted cracking behavior of AA7075-T651 in aqueous NaCl solution. Cor. Mater. Degrad. 2021;2:360–75. https://doi.org/10.3390/cmd2030019.

[55] McMahon ME, Steiner PJ, Lass AB, Burns JT. The effect of temper and composition on the stress corrosion cracking of Al-Mg alloys. Corrosion 2017;73:347–61. https://doi.org/10.5006/2317.

[56] Somerday BP, Young LM, Gangloff RP. Crack tip mechanics effects on environment-assisted cracking of beta-titanium alloys in aqueous NaCl. Fatigue Fract Eng Mater Struct 2000;23:39–58. https://doi.org/10.1046/j.1460-2695.2000.00243.x.

[57] E647-15e1. Standard Test Method for Measurement of Fatigue Crack Growth Rates. ASTM Book of Standards 2016:1–49. https://doi.org/10.1520/E0647-15E01.2.

[58] ABAQUS/Standard 2021 Reference Manual, 2021.

[59] FRANC3D Reference Manual, Version 7.5, 2020.

[60] Banks-Sills L, Hershkovitz I, Wawrzynek PA, Eliasi R, Ingraffea AR. Methods for calculating stress intensity factors in anisotropic materials: Part I—z=0 is a symmetric plane. Eng. Fract. Mech. 2005;72:2328–58. https://doi.org/10.1016/j.engfracmech.2004.12.007.

[61] Harris ZD, Dubas EM, Schrock DJ, Locke (Warner) JS, Burns JT. Assessing the fatigue crack growth behavior of highly sensitized AA5456-H116 under cathodic polarization. Mater. Sci. Engng. A 2020;139792. https://doi.org/10.1016/j.msea.2020.139792.

[62] Clark W, Hudak S. Variability in fatigue crack growth rate testing. J. Test Eval. 1975;3:454–76. https://doi.org/10.1520/JTE11702J.

[63] Anderson TL. Fracture Mechanics: Fundamentals and Applications. 3rd ed. Taylor & Francis; 2005.

[64] Hudak Jr. SJ, Bucci RJ, editors. ASTM, editors. STP 738: Fatigue Crack Growth Measurement and Data Analysis. Philadelphia, PA: ASTM; 1981.

[65] Suresh S. Fatigue of Materials. 2nd ed. Cambridge, UK: Cambridge University Press; 1998.

[66] Pippan R, Hohenwarter A. Fatigue crack closure: a review of the physical phenomena. Fatigue Fract Eng Mater Struct 2017;40:471–95. https://doi.org/10.1111/ffe.12578.

[67] Hutchinson JW. Singular behaviour at the end of a tensile crack in a hardening material. J. Mech. Phys. Solids 1968;16:13–31.

[68] Rice JR, Rosengren GF. Plane strain deformation near a crack tip in a power-law hardening materials. J. Mech. Phys. Solids 1968;16:1–12.

[69] John R, Rigling B. Effect of height to width ratio on K and CMOD solutions for a single edge cracked geometry with clamped ends. Eng. Fract. Mech. 1998;60:147–56. https://doi.org/10.1016/S0013-7944(98)00009-5.

[70] Van Stone RH. Private Communication 2023.

[71] Bomarito GF, Townsend T, Hochhalter JD, Adams E, Esham K, Vera D. BINGO 2018. https://github.com/nasa/bingo.

[72] Galyon Dorman SE, Niebuhr JH, Locke JS, Free B. Paper No. 2019-0218-0314-000077: The Development of a Method for Complex Environment Corrosion Fatigue Testing. 2019 DoD-Allied. Nations Technical Corrosion Conference; 2019.

[73] McMahon ME, Harris ZD, Scully JR, Burns JT. The effect of electrode potential on stress corrosion cracking in highly sensitized Al–Mg alloys. Mater. Sci. Engng. A 2019;767:138399. https://doi.org/10.1016/j.msea.2019.138399.

[74] Crane CB, Kelly RG, Gangloff RP. Crack chemistry control of intergranular stress corrosion cracking in sensitized Al-Mg. Corrosion 2016;72:242–63. https://doi.org/10.5006/1852.

[75] Burns JT, Harris ZD, Dolph JD, Gangloff RP. Measurement and modeling of hydrogen environment assisted cracking in a Ni-Cu-Al-Ti superalloy. Metall. Mater. Trans. A 2016;47:990–7. https://doi.org/10.1007/s11661-015-3315-4.

[76] Harris ZD, Dolph JD, Pioszak GL, Rincon Troconis BC, Scully JR, Burns JT. The effect of microstructural variation on the hydrogen environment-assisted cracking of Monel K-500. Metall. Mater. Trans. A 2016;47:3488–510. https://doi.org/10.1007/s11661-016-3486-7.

[77] Harris ZD, Burns JT. The effect of isothermal heat treatment on hydrogen environment-assisted cracking susceptibility in Monel K-500. Mater. Sci. Engng. A 2019;764:138249. https://doi.org/10.1016/j.msea.2019.138249.

[78] Harris ZD, Dubas EM, Popernack AS, Somerday BP, Burns JT. Elucidating the loading rate dependence of hydrogen environment-assisted cracking in a Ni-Cu superalloy. Theor. Appl. Fract. Mech. 2021;111:102846. https://doi.org/10.1016/j.tafmec.2020.102846.

[79] Harris ZD, Guiseva K, Scully JR, Burns JT. On the hydrogen environment-assisted cracking resistance of a compositionally complex Co–Ni–Cr–Fe–Mo–Ti alloy. Mater. Sci. Engng. A 2020;802:140601. https://doi.org/10.1016/j.msea.2020.140601.

[80] Harris ZD, Burns JT. On the loading rate dependence of environment-assisted cracking in sensitized AA5456-H116 exposed to marine environments. Corros Sci 2022;201:110267. https://doi.org/10.1016/j.corsci.2022.110267.

[81] Steiner PJ, Harris ZD, Vicente Moraes C, Kelly RG, Burns JT. Investigation of IG-SCC growth kinetics in Al-Mg alloys in thin film environments. Corrosion 2021. https://doi.org/10.5006/3833.

[82] McMahon ME, Steiner PJ, Lass AB, Burns JT. The effect of loading orientation on the stress corrosion cracking of Al-Mg alloys. Corrosion 2017;73:713–23. https://doi.org/10.5006/2343.

[83] Harris ZD, Marshall RS, Kelly RG, Burns JT. Coupling fracture mechanics experiments and electrochemical modeling to mitigate environment-assisted cracking in engineering components. Corrosion 2023;79:363–75.